



**HAL**  
open science

# Multiplatform observations of the seasonal evolution of the Saharan atmospheric boundary layer in Tamanrasset, Algeria, in the framework of the African Monsoon Multidisciplinary Analysis field campaign conducted in 2006

Juan Cuesta, Dimitri Edouart, Mohamed Mimouni, Pierre H. Flamant, Claude Loth, Fabien Gibert, Fabien Marnas, Abdelkrim Bouklila, Mohamed Kharef, Bouziane Ouchène, et al.

## ► To cite this version:

Juan Cuesta, Dimitri Edouart, Mohamed Mimouni, Pierre H. Flamant, Claude Loth, et al.. Multiplatform observations of the seasonal evolution of the Saharan atmospheric boundary layer in Tamanrasset, Algeria, in the framework of the African Monsoon Multidisciplinary Analysis field campaign conducted in 2006. *Journal of Geophysical Research: Atmospheres*, 2008, 113 (D23), pp.D00C07. 10.1029/2007JD009417 . hal-00311302

**HAL Id: hal-00311302**

**<https://hal.science/hal-00311302>**

Submitted on 4 Feb 2016

**HAL** is a multi-disciplinary open access archive for the deposit and dissemination of scientific research documents, whether they are published or not. The documents may come from teaching and research institutions in France or abroad, or from public or private research centers.

L'archive ouverte pluridisciplinaire **HAL**, est destinée au dépôt et à la diffusion de documents scientifiques de niveau recherche, publiés ou non, émanant des établissements d'enseignement et de recherche français ou étrangers, des laboratoires publics ou privés.

# Multiplatform observations of the seasonal evolution of the Saharan atmospheric boundary layer in Tamanrasset, Algeria, in the framework of the African Monsoon Multidisciplinary Analysis field campaign conducted in 2006

Juan Cuesta,<sup>1</sup> Dimitri Edouart,<sup>1</sup> Mohamed Mimouni,<sup>2</sup> Pierre H. Flamant,<sup>1</sup> Claude Loth,<sup>1</sup> Fabien Gibert,<sup>1</sup> Fabien Marnas,<sup>1</sup> Abdelkrim Bouklila,<sup>2</sup> Mohamed Kharef,<sup>2</sup> Bouziane Ouchène,<sup>2</sup> Mohamed Kadi,<sup>3</sup> and Cyrille Flamant<sup>4</sup>

Received 25 September 2007; revised 17 May 2008; accepted 29 May 2008; published 5 August 2008.

[1] We document the seasonal evolution of the Saharan atmospheric boundary layer (SABL), in terms of vertical structure, diurnal cycle, aerosol content, and cloud cover as well as the surface radiative budget, during 2006, using a mobile multiplatform atmospheric observatory implemented in Tamanrasset (Algeria). Ground-based remote sensing (both active and passive) and in situ instruments were deployed in the framework of the African Monsoon Multidisciplinary Analysis field experiment and were used in synergy with satellite observations. Observations showed a marked seasonal evolution of the SABL characteristics and a large variability during the West African monsoon onset phase. At the beginning of June, hazy conditions prevailed in a deep SABL (~5 km). Following this, reduced cloud cover induced by anomalous large-scale subsidence resulted in high surface insolation which enhanced the convective development of the SABL (~6 km deep). During that period, the proximity of the Saharan heat low was also favorable to the SABL deepening. In August and September, humidity advected from the south enhanced cloud cover and limited the SABL vertical development (~3.8 km deep). In the wintertime, weak dry convection and the Hadley cell–related subsidence resulted in high visibility and an extremely shallow SABL (~500 m deep). Throughout 2006, the aerosol vertical distribution within the SABL was nonuniform, with the majority of coarse particles being located near the surface. The aerosol content over Tamanrasset was influenced by dust transport from a variety of source regions after being lifted through different mechanisms (low-level jets; cold pools or topographic flows).

**Citation:** Cuesta, J., et al. (2008), Multiplatform observations of the seasonal evolution of the Saharan atmospheric boundary layer in Tamanrasset, Algeria, in the framework of the African Monsoon Multidisciplinary Analysis field campaign conducted in 2006, *J. Geophys. Res.*, 113, D00C07, doi:10.1029/2007JD009417.

## 1. Introduction

[2] An international field campaign was conducted in West Africa during 2006 under the African Monsoon Multidisciplinary Analysis (AMMA) framework [Redelsperger *et al.*, 2006]. The objective of AMMA is to improve our current knowledge of physical and dynamical processes, with an emphasis on daily to interannual time scales, for a better understanding and prediction of the West African monsoon (WAM) cycle. Furthermore, AMMA is

motivated by the impact of the WAM on water resources, the main driver for health and food security of populated regions of West Africa. Indeed, the economy of most countries in the Sahel region (the semidesert southern fringe of the Sahara that stretches from Mauritania to Chad) relies on small-scale agricultural production that depends on the occurrence and amount of precipitation during the WAM season. A particularly crucial issue is the low “efficiency” of cloud systems in terms of “useful rain” as well as the occurrences of dry spells during the monsoon season that may lead to the destruction of crops [Ati *et al.*, 2002].

[3] The seasonal cycle of the WAM is closely linked to the energy balance in the Sahara [e.g., Ramel *et al.*, 2006; Peyrillé and Lafore, 2007; Peyrillé *et al.*, 2007], and particularly in the Saharan atmospheric boundary layer (SABL). In the summer, the SABL is characterized by the presence of a deep and dense dust layer which, in combination with high soil temperature, constitutes a unique destabilizing factor [Bounoua and Krishnamurti, 1991]

<sup>1</sup>Laboratoire de Météorologie Dynamique, Institut Pierre Simon Laplace, École Polytechnique, Palaiseau, France.

<sup>2</sup>Centre Tamanrasset, Office National de la Météorologie, Tamanrasset, Algeria.

<sup>3</sup>Centre Alger, Office National de la Météorologie, Algiers, Algeria.

<sup>4</sup>Service d'Aéronomie, Institut Pierre Simon Laplace, Paris, France.

which drives the Saharan heat low (SHL) dynamics. In response to the large scale pressure gradient between the SHL and the Gulf of Guinea, the monsoon flow may penetrate deeply into the continent. It reaches the Sahel at the end of June or in early July, thereby favoring the appearance of convective systems and the beginning of the rainy season in Sahel (also referred to as the “monsoon onset”) [Sultan and Janicot, 2000]. Hence, the SABL is a complex element of the climate of the West African region which needs to be more rigorously investigated given the paucity of observations in the area. Improved knowledge of the energy balance in the SABL requires concomitant monitoring of the radiation budget, the aerosol optical/microphysical properties and their vertical distribution in the troposphere, as well as the SABL structural parameters which affect the vertical distribution both of aerosols and thermodynamics variables.

[4] The SABL is of central importance in the AMMA project. An ambitious experimental strategy which involved balanced contributions from ground-based and airborne platforms was tailored in 2006 as part of the AMMA Special Observing Period (SOP) [Parker and Flamant, 2006]. The objective of the ground-based component of the experimental strategy was to document the diurnal cycle and the seasonal evolution of relevant variables (structure, thermodynamics, radiation, etc. . .) over the Sahara. Spaceborne observations of cloud cover and aerosol layers, relevant to the understanding of the SABL dynamics at the mesoscale, have been enhanced since the launch in late April 2006 of the CALIPSO (Cloud-Aerosol Lidar and Infrared Pathfinder Satellite Observation) mission [Winker et al., 2003, 2007].

[5] The present paper presents an overview of the SABL observations performed at the Tamanrasset supersite, Algeria (22.79°N, 5.53°E), in 2006. This work was conducted in collaboration between the Institut Pierre Simon Laplace (IPSL) in France and the Office National de la Météorologie (ONM) in Algeria. The Division Sud of the ONM operates a suite of instruments in Tamanrasset (in the heart of the Sahara) which was enhanced by the deployment of the IPSL atmospheric mobile observatory MOBILIS (Moyens Mobiles de Télédétection de l’IPSL). MOBILIS included a ground-based backscatter lidar, an AERONET (Aerosol Monitoring Network) [Holben et al., 1998] Sun photometer and infrared radiometers, both deployed for the first time in the Sahara, as well as meteorological and aerosol-related in situ instrumentation. The Tamanrasset supersite was the northernmost experimental site implemented in the framework of AMMA. It was dedicated to the documentation both of the diurnal cycle and the seasonal evolution of the SABL. The choice of the site of Tamanrasset for the implementation of MOBILIS was made considering both logistical constraints (not to be neglected in Africa) as well as the wealth of the already existing ONM instrumentation. The Tamanrasset supersite was therefore equipped to study (1) the vertical structure and diurnal cycle of the SABL, (2) the Saharan dust optical properties and radiative forcing, and (3) the interaction with the SHL dynamics, related to the WAM cycle, in synergy with airborne and spaceborne observations. Furthermore, the MOBILIS deployment was intended to contribute to the CALIPSO validation effort.

[6] Section 2 describes the IPSL and ONM instrumentation deployed in Tamanrasset, and the complementary spaceborne data sets used in the present study (i.e., CALIPSO, the Spinning Enhanced Visible and Infra Red Imager (SEVIRI), the Moderate Resolution Imaging Spectroradiometer (MODIS), and the Ozone Monitoring Instrument (OMI)). Section 3 presents an overview of the main WAM phases and the periods of operations on the Tamanrasset supersite. Section 4 presents an overview of the meteorological conditions prevailing in Tamanrasset during AMMA 2006. Section 5 describes the seasonal evolution in 2006 of the SABL over Tamanrasset, i.e., vertical structure, dust content, cloud cover and surface energy balance. Section 6 presents detailed case studies to illustrate the evolution of the structure and diurnal cycle of the SABL during the year. Concluding remarks are given in section 7.

## 2. Experimental Deployment and Data Sets

### 2.1. Multi-Instrumented Supersite in Tamanrasset

[7] The MOBILIS facility was deployed in Tamanrasset from February to November 2006, during the AMMA SOP [Redelsperger et al., 2006] and beyond. The core instrumentation of the MOBILIS facility is the Transportable Remote Sensing Station (TReSS) [Cuesta et al., 2004; Loth et al., 2004] which includes an in-house designed and built multiwavelength backscatter MiniLidar, which is used in synergy with radiometers and in situ sensors (see Table 1). The instrumentation of the ONM station in Tamanrasset is dedicated to the monitoring of meteorological variables as well as the radiative budget at the surface. Table 1 summarizes the main characteristics (type of measurements, resolution, accuracy, etc) of the MOBILIS and ONM instruments operated at the Tamanrasset supersite.

[8] Tropospheric lidar measurements have largely been used to describe boundary layer dynamics [e.g., Flamant et al., 2007], including the boundary layer diurnal cycle, vertical mixing processes or wave-like phenomena. Lidar profiles also provide information on aerosol and cloud vertical distributions and optical properties. Indicators of the concentration, shape and size of backscattering particles are given by the attenuated backscattered coefficient, the depolarization ratio and the color ratio profiles, respectively (see Table 1 for details). The attenuated backscattered coefficient is a function of the backscatter coefficient profile  $\beta(z)$ , which depends on the concentration and backscatter cross section of the scattering components in the atmosphere (i.e., molecules, aerosols and hydrometeors), times the two-way atmospheric transmission  $T^2$ . The attenuated backscatter coefficient ( $\beta T^2$ , expressed in  $\text{sr}^{-1} \text{m}^{-1}$ ) is derived from the TReSS and CALIPSO lidars (see section 2.2). Considering the different instrumental noises in the TReSS lidar data, the uncertainty in calibration of the attenuated backscatter coefficient (see section 6.1) is estimated as  $\sim 5\%$  (see Table 1). Random noise from 150 m (the full overlap altitude) to 4.5 km above ground level (AGL) typically remains below 3% (for the 30-min averaged profiles). In order to derive the backscatter coefficient profile  $\beta(z)$  (see section 6), a standard backscatter lidar inversion technique [Fernald et al., 1972; Fernald, 1984] is implemented to compute the atmospheric transmission  $T^2$  and correct for atmospheric attenuation.

**Table 1.** Description of the Instrumental Payload of the Atmospheric Mobile Observatory MOBILIS and of the ONM facility in Tamanrasset<sup>a</sup>

Instrument Number	Instrument	Affiliation	Operation	Characteristics	Products
1	backscatter minilidar	TReSS	IOP	<i>Active Remote Sensing</i> vertical profiles; four channels (532 linear and cross polarization, 1064 and 607 nm Raman); resolution of 30 m x 30 s; full overlap above 150 m AGL; uncertainty of <5% in normalization (at 4.5 AGL) and <3% in random noise (for 30 min-average profiles and up to 5 AGL)	attenuated backscatter at 532 and at 1064 nm (the ratio constitutes the color ratio); depolarization ratio (between linear and cross-polarization returns) at 532 nm; particle extinction at 607 nm
2	Sun photometer	TReSS	C	<i>Passive Remote Sensing</i> model: CIMEL CE-318; column-integrated daytime measurements; six channels (440, 500, 670, 870, 936 and 1020 nm); narrowband (20 nm); spheroid almuicantar algorithm for size distribution and SSA retrieval; uncertainty of <0.01 for AOD and <0.03 for SSA	aerosol optical depth (AOD); single scattering albedo (SSA); volume size distribution; integrated water content
3	radiative flux station	ONM	R	downwelling wideband radiative fluxes at the surface; uncertainty of <3 W m <sup>-2</sup> d <sup>-1</sup>	
3.1	pyranometer			spectral band: 0.3–3.2 μm	global shortwave radiance
3.2	periheliometer			spectral band: 0.3–3.2 μm	direct solar radiance
3.3	pyrgeometer			spectral band: 4.5–42 μm	longwave radiance
4	wide-angle camera	TReSS	IOP	zenith view; web-type camera	cloud cover
5	scatterometer	L/C	IOP	<i>In Situ</i> model: MIE RAM1; sampling 3 m from the surface; one narrowband channel (920 nm); uncertainty of <10%	particle scattering coefficient
6	optical particle counter	MOB	C	model: GRIMM 108.0; sampling 4 m from the surface; 15 classes for 0.15 μm < r < 10 μm; time resolution of 6 s; uncertainty of <3% in maximum range	particle number size distribution
7	ultrasonic anemometer	MOB	C	<i>Meteorological Variables</i> model: Campbell CSAT3; at 10 m from the surface; sampling frequency of 60 Hz; sensible heat flux estimated by covariance calculation within 5 min of vertical speed and sonic temperature; uncertainty of <4 cm s <sup>-1</sup> (horizontal wind), <2 cm s <sup>-1</sup> (vertical speed) and 3% (sensible heat flux)	wind components; sensible heat flux and friction velocity; sonic temperature
8	radiosondes	ONM	R	model: Vaisala RS92; 2 per day (0000 UTC and 1200 UTC) in routine operation and +2 per day (0600 UTC and 1800 UTC) during AMMA SOPs; launching platform located 8 km from TReSS site	pressure, temperature, humidity and wind profiles
9	temperature and humidity sensor	MOB	C	model: Vaisala MP45D/HMP45A; at 10 m from the surface; time resolution of 10 s	temperature, humidity
10	pressure sensor	ONM	R	at 2 m from the surface; time resolution of 3 h	surface pressure

<sup>a</sup>The second column indicates the affiliation of each instrument: “TReSS” or “MOB” (MOBILIS) for instruments developed at the Institut Pierre Simon Laplace (IPSL) France, “L/C” for the Laboratoire des Sciences du Climat et l’Environnement/Commissariat à l’Énergie Atomique, Saclay (France) and “ONM” (Algeria). The third column specifies the mode of operation: “IOP” for operator assisted operations during IOPs, “C” for continuous operations, and “R” for ONM routine operations. The TReSS Sun photometer was affiliated to the AERONET network during the year 2006 (<https://aeronet.gsfc.nasa.gov/>).

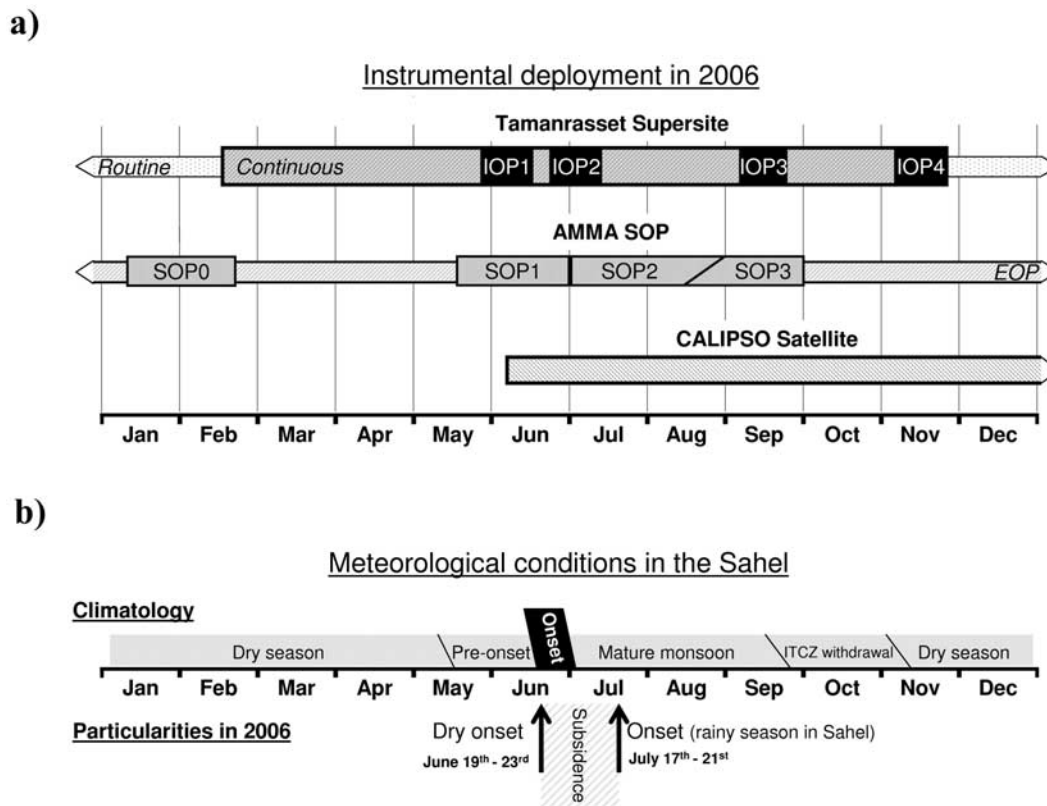


**Figure 1.** (a) Calendar of observations performed in the framework of the AMMA SOP in 2006 for the Tamanrasset Supersite, AMMA campaign (<http://amma-international.org>) [Parker and Flamant, 2006] and CALIPSO Satellite (<http://eosweb.larc.nasa.gov/>). (b) Description of the main WAM phases (climatology and specificity of the year 2006).

[9] Column-averaged/surface optical and microphysical aerosol properties were obtained via the Sun photometer/in situ sensors. Wideband radiometers (instrument 3 in Table 1) monitored the downwelling solar (direct and diffuse components) and telluric fluxes at the surface. The surface sensible heat flux was derived from ultrasonic anemometer measurements of wind and temperature (instrument 7 in Table 1) [Schotanus *et al.*, 1983]. During unstable and dry conditions, such as those prevailing in Tamanrasset during daytime, the bias produced by this method was estimated to be as low as 3% [Schotanus *et al.*, 1983]. No latent heat flux measurements were available. For arid regions [Heusinkveld *et al.*, 2004], a rough estimation based on a Bowen ratio method [Stull, 1988] suggests that the latent heat flux in Tamanrasset is about 10 to 20% of the sensible heat flux. Moreover, a surface energy closure analysis (see section 5.2) suggests that the contribution of the latent heat flux remained below the daily variability of the other fluxes (particularly in absence of rainfall). Additionally, radiosoundings (instrument 8 in Table 1) provided the atmospheric thermodynamic structure every 6 h during the summer AMMA SOPs (1 June to 15 September), and twice a day, at synoptic times, for the remaining of the year.

[10] During the 9 months of AMMA-related operations, the instruments in Tamanrasset ran according to three modes (see Table 1 and Figure 1a): (1) routine operations for the ONM instrumentation (instruments 3, 8 and 10 in Table 1); (2) continuous operations for the MOBILIS Sun photometer

(instrument 2 in Table 1), aerosol in situ sampling devices (instrument 6 in Table 1), sonic anemometer (instrument 7 in Table 1) and meteorological station (instrument 9 in Table 1); and finally (3) intensive operations in the framework of 2- to 3-week-long Intensive Observation Periods (IOPs, see Figure 1) for the MOBILIS lidar (instrument 1 and Table 1), scatterometer (instrument 4 and Table 1) and wide-angle camera (instrument 5 in Table 1). The harsh meteorological conditions in Tamanrasset (heat, dust, etc) made it difficult for the lidar to be continuously operational during the entire AMMA-related detachment. Further details on the daily instrument status can be found in the auxiliary material to this paper.<sup>1</sup>

## 2.2. CALIPSO Spaceborne Lidar

[11] The CALIPSO satellite was launched in April 2006 and started operating in June (see Figure 1a). The CALIPSO payload consists of the Cloud-Aerosol Lidar with Orthogonal Polarization (CALIOP), the Infrared Imaging Radiometer (IIR) and the Wide Field Camera (WFC) [Winker *et al.*, 2003, 2007]. CALIPSO overpasses the Sahara twice a day, once during the daytime (between 1230 and 1430 UTC, Coordinated Universal Time) and once during the nighttime (between 0030 and 0230 UTC), and has a revisit time period of the same orbit of 16 days. Each overpass of the

<sup>1</sup>Auxiliary materials are available in the HTML. doi:10.1029/2007JD009417.

CALIOP lidar provides a quasi-instantaneous view of the vertical structure of dust plumes and of the SABL across the Sahara (i.e., between 15°N to 35°N in less than 5 min). Tamanrasset is located approximately 15 km east of the intersection between an ascending (daytime) track and a descending (nighttime) track of CALIPSO. In this study, the CALIOP data are used to provide complementary meso-scale context to the TReSS lidar measurements.

### 2.3. SEVIRI, MODIS, and OMI

[12] The origin and transport pathways of dust plumes arriving at Tamanrasset are investigated using complementary satellite imagery. Qualitative tracking of dust plumes over the Sahara is done using observations from SEVIRI (15 min. temporal resolution) onboard MSG (Meteosat Second Generation) via false color images available from (<http://loamma.univ-lille1.fr/AMMA/>). Semiquantitative aerosol indices (AI) provided daily by OMI (<http://toms.gsfc.nasa.gov>) are also used.

[13] The upwelling longwave and shortwave radiative fluxes in Tamanrasset are estimated using MODIS retrievals of the surface albedo  $\omega$  and emissivity  $\varepsilon$  (i.e., MODIS land products with a 1-km horizontal resolution, <http://edcdaac.usgs.gov/dataproducts.asp>). These estimates are used, together with the surface radiative and turbulent fluxes measurements, to verify the closure of the surface energy budget in Tamanrasset (see section 5.2).

### 3. WAM Phases and IOPs in Tamanrasset

[14] The seasonal evolution of the SABL over the Sahara, and in Tamanrasset, is strongly influenced by the seasonal cycle of the WAM and that of the SHL. This section gives some large-scale seasonal context to the observations made in Tamanrasset which are detailed in sections 4 to 6.

[15] The annual cycle of the WAM is characterized by phases which indicate the state of the WAM over Sahel (see Figure 1b). The preonset phase corresponds to the arrival of the intertropical discontinuity (ITD) over Sahel and marks the end of the dry season. The ITD is the near surface convergence zone between the harmattan, originating from the eastern Mediterranean and passing over the deserts of Libya, Egypt and Algeria, and the moist monsoon flow coming from the Gulf of Guinea. The climatological date for preonset occurrence is 14 May  $\pm 9.5$  days [Sultan and Janicot, 2003]. The monsoon onset phase, which corresponds to the beginning of the rainy season in the Sahel, occurs typically around 24 June, with a variability of  $\pm 8$  days [Sultan and Janicot, 2000, 2003]. The mature monsoon phase is then observed over Sahel which typically lasts until the middle of September. In this period the intertropical convergence zone (ITCZ) is positioned around 10°N, and the monsoon exhibits its northward most excursions, sometimes reaching the Ahaggar massif. Finally, a transition phase toward the dry season is observed while the ITCZ retreats southward, and the rainy season comes to an end.

[16] In 2006, the main WAM phases were consistent with the climatological picture, except for the onset phase. Enhanced subsidence over the whole of West Africa, during three weeks at the end of June and the beginning of July, led to a “dry onset” (meaning that all the indicators suggested the onset had occurred, except for the rain) around the climato-

logical date (between 19 to 23 June) and delayed the beginning of the rainy season over Sahel by nearly a month, i.e., sometime between 17 and 21 July [Janicot and Sultan, 2007].

[17] As shown in Figure 1, the IOPs in Tamanrasset were designed to sample the SABL during each of the WAM phases. IOP 1 (25 May to 17 June) occurred during the WAM preonset phase. As shown in section 5.1, this period was favorable for intense dust transport episodes in the Tamanrasset region. IOP 2 (25 June to 11 July) took place during the period of enhanced subsidence, just prior to the monsoon onset, which lead to the observation of strong dry convection in Tamanrasset (see section 5.3). IOP 3 (7–21 September) and IOP 4 (5–23 November) happened during the mature monsoon phase and in the ITCZ withdrawal period, respectively. IOP 3 was associated with monsoon-related moisture advection episodes, while shallow convection conditions were observed during IOP 4 (see sections 4.2 and 6.4, respectively).

### 4. Meteorological Conditions Prevailing Over Tamanrasset in 2006

[18] Tamanrasset is located in the middle of the Sahara, in the heart of the Ahaggar massif at 1370 m above the mean sea level (MSL) and 65 km south of the tropic of Cancer. This region is under the influence of the Mediterranean weather for the most part of the year, and is affected by the WAM during a short period in the summertime [Dubief, 1979]. Furthermore, the SHL is located to the west of Tamanrasset during the summer (June, July, and August) and interacts with the northward progression of the monsoon, that eventually approaches the Ahaggar.

[19] Figure 2 presents the meteorological conditions over West Africa during the WAM phases in 2006, based on European Center for Medium-range Weather Forecasts (ECMWF) analyses. Prior to the WAM dry onset, the ITD is located south of the Tropic of Cancer at least 700 km south of Tamanrasset (see Figure 2b). The core SHL region (delineated using the  $\leq 1006$  hPa isocontour in Figure 2a) is then positioned south of the Ahaggar massif. Just before the monsoon onset, the SHL shifts from a position south of the Ahaggar massif (Figure 2a) to a position west of the Ahaggar massif (Figure 2c). Similarly, the ITD progresses northward, reaching the Air Massif. Nevertheless, strong easterly winds are observed in the lee of the constriction between the Air and Ahaggar mountains that prevent the monsoon from reaching the Ahaggar. Finally, after the onset, a well established SHL is fairly close to Tamanrasset (Figure 2e). The ITD exhibits its northernmost position over Mali and Mauritania up to the Algerian border (mean location over 15 days, see Figure 2f), consistent with the position of the SHL. During this period, some parts of the ITD were as close as 200 km southwest of Tamanrasset (Figure 2f). It is also worth noting that during the mature monsoon phase, the strong cyclonic circulation associated with the SHL favors the advance of the monsoon onto the foothills of the Ahaggar. The influence of the SHL is observed in the surface pressure measurements made in Tamanrasset (Figure 3a). After the beginning of July, the influence of the SHL in Tamanrasset is marked by a  $\sim 4$  hPa decrease in the surface pressure (see Figure 3a and section 5.3 for further discussion) with a concomitant maximum in

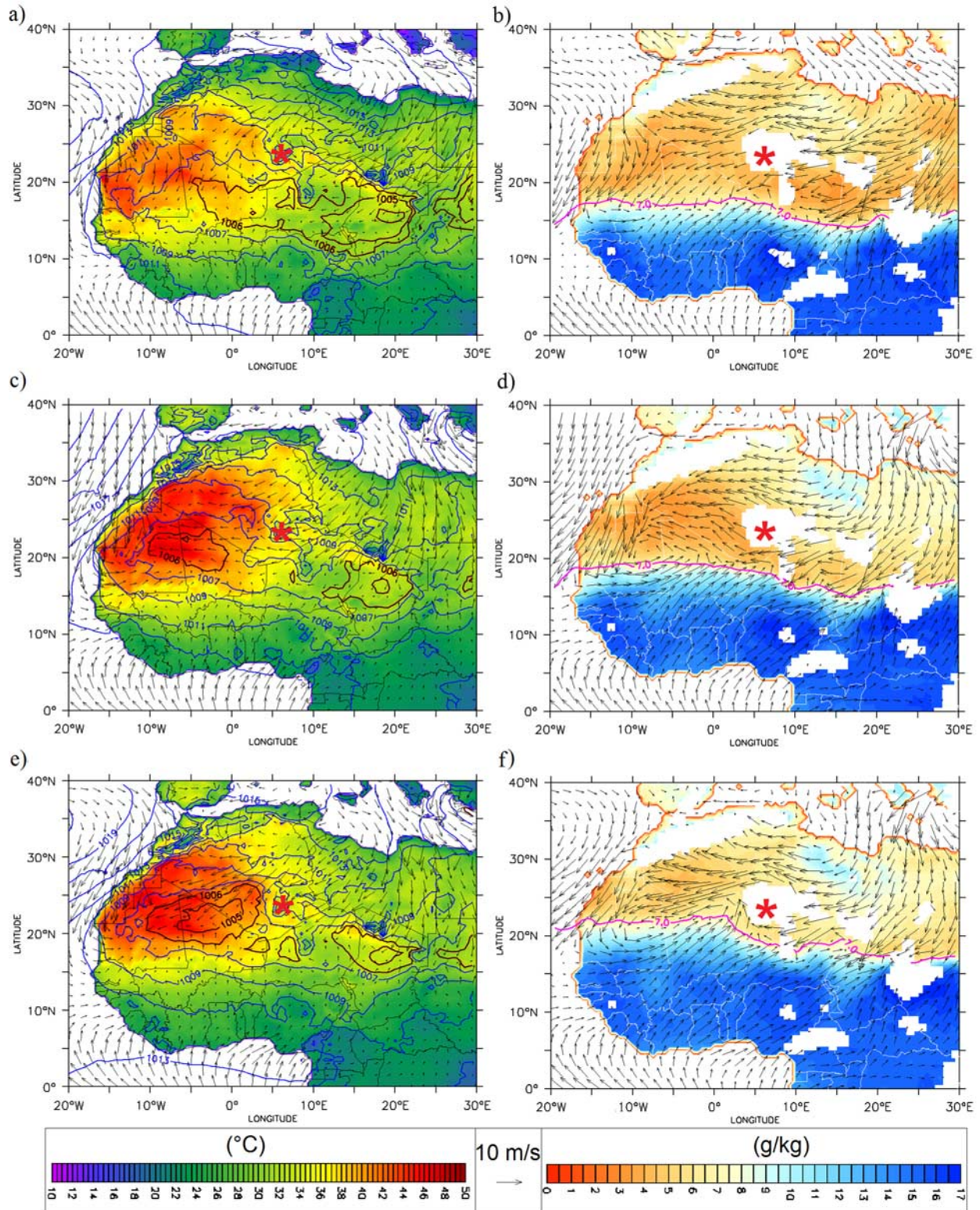


**Figure 2.** ECMWF analyses over West Africa for the following periods: (a and b) 1–15 June, (c and d) 1–15 July, and (e and f) 16–31 July. Figures 2a, 2c, and 2e display surface temperature (color), mean sea level pressure (blue and black contours in hPa), and 10 m wind fields (arrows) at 1800 UTC. The SHL structure is depicted, in first approximation, by pressures less than 1006 hPa. Water vapor mixing ratio (color) and wind fields at 925 hPa (arrows) at 0600 UTC are presented in Figures 2b, 2d, and 2f. The ITD location as determined from the 7 g/kg water vapor mixing ratio isocontour (magenta line) is also shown. The orography at the 925 hPa level is shown in white. The location of Tamanrasset is indicated by a red star.

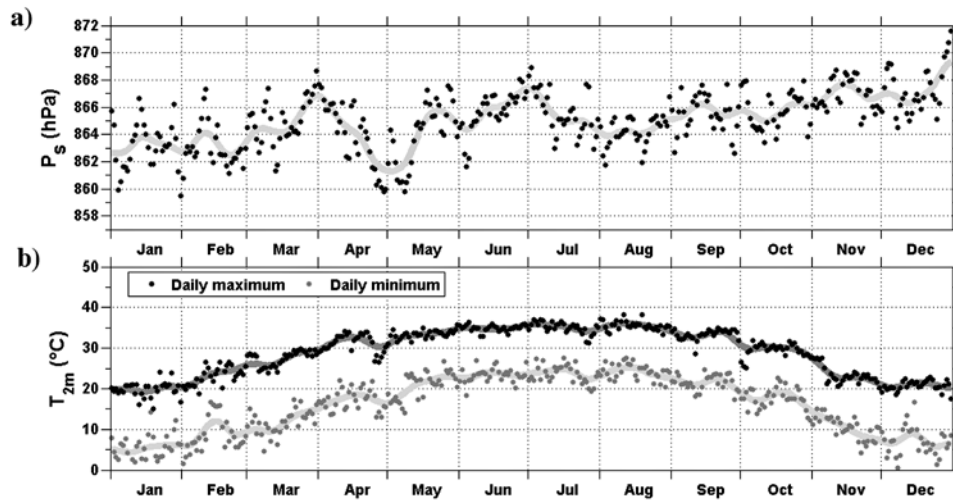


**Figure 3.** (a) Surface pressure  $P_S$  and (b) temperature at 2 m  $T_{2m}$  in Tamanrasset in 2006. The daily MAXima and minima of  $T_{2m}$  as well as the daily mean values of  $P_S$  are indicated by dots. Low-pass filtered data obtained with a 10-day sliding window are shown by solid gray lines.

surface temperature (see Figure 3b). The minimum of surface pressure and the maximum of surface temperature observed during the summer coincide with the period when the SHL is strongest over the Sahara (C. Lavaysse et al., Seasonal cycle of the West African heat low: A climatological perspective, submitted to *Climate Dynamics*, 2008).

[20] On the other hand, the surface pressure minima observed in Tamanrasset during the winter are associated with the passage of midlatitude depressions. The strongest event is observed at the end of April and beginning of May (as a surface pressure decrease of  $\sim 5$  hPa) and is linked to a

succession of three midlatitude depressions (according to ECMWF analysis).

#### 4.1. Wind Regimes

[21] Figure 4 shows the seasonal evolution of wind speed and wind direction over Tamanrasset during 2006, constructed from balloon sounding measurements (4 soundings per day from 1 June to 15 September and 2 soundings per day otherwise). Two markedly different circulation regimes are observed in the wintertime and in the summertime. From October to May, westerly winds are present from 2 to 20 km MSL, typically coupled to midlatitude low-pressure systems

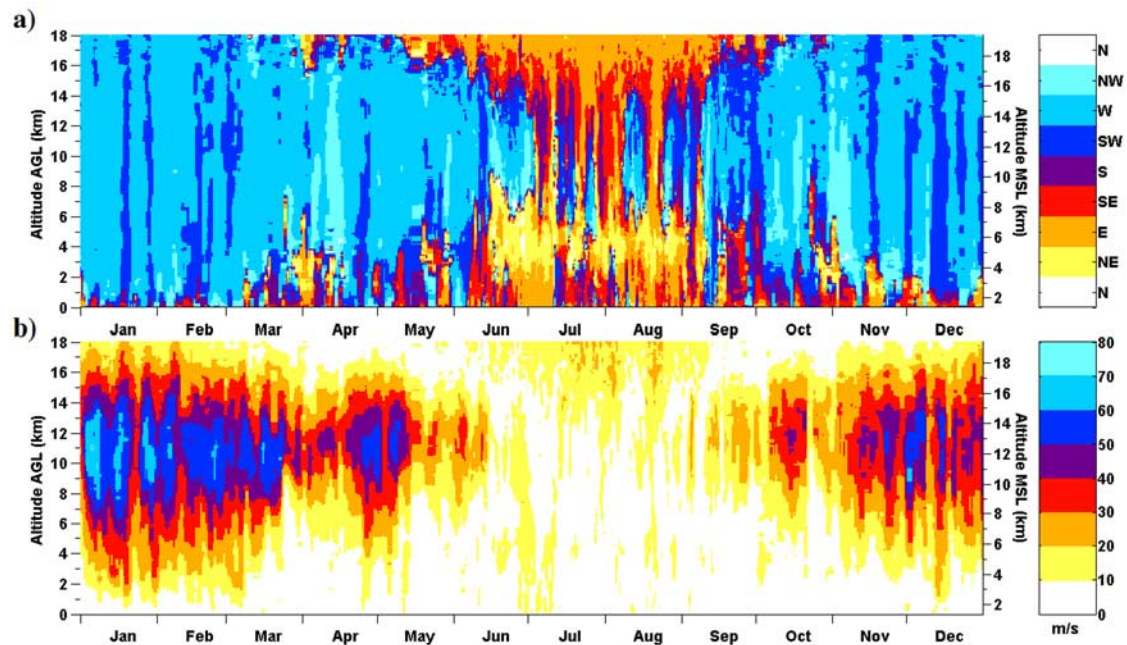


**Figure 4.** (a) Horizontal wind direction and (b) wind speed over Tamanrasset in 2006. The wind profiles were measured by radiosondes (four per day from June to September and two per day outside this period).

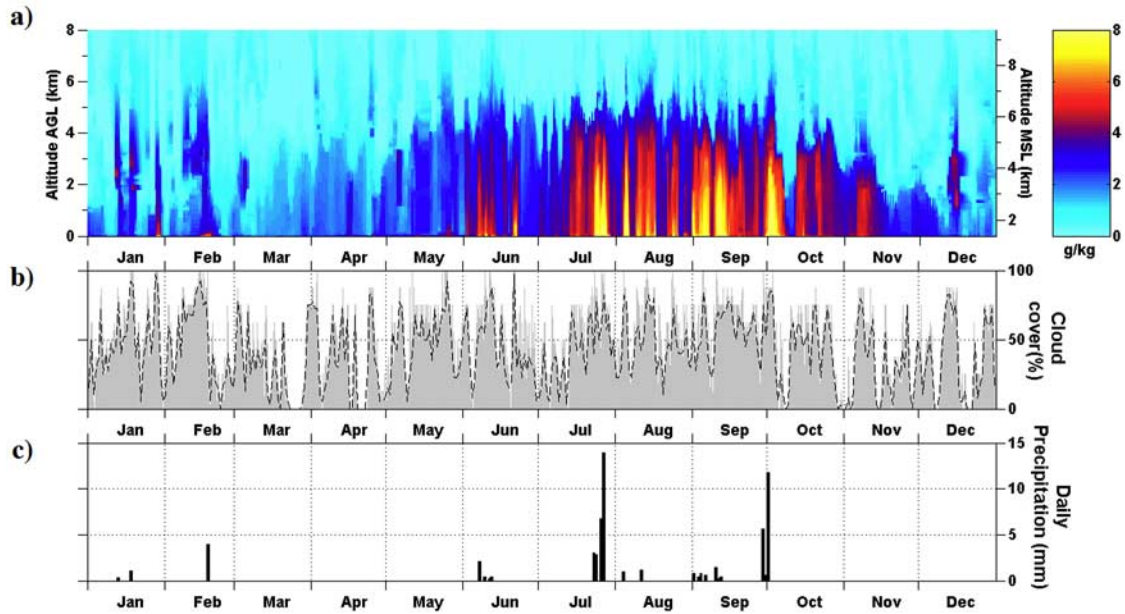


**Figure 5.** (a) Water vapor mixing ratio, (b) cloud cover, and (c) daily precipitation over Tamanrasset in 2006. Cloud cover (Figure 5b) is the fraction of the sky covered by clouds, estimated by visual inspection of an ONM ground observer (at 0600, 0900, 1200, 1500, and 1800 UTC), expressed in percentage (gray shading). Daily averaged values are given by the dashed line.

[Dubief, 1979]. They are associated with the Subtropical Westerly Jet (STWJ), which is observed between 7 to 16 km MSL (see Figure 4b). In the summertime, from June to September, the circulation regime changes completely. At higher altitudes (above 15 km MSL), easterly winds (20 m/s or less) are observed because of the influence of the northern edge of the Tropical Easterly Jet (TEJ) positioned over the Guinean coast. From 9 to 15 km MSL, westerly winds are also observed which are periodically disrupted by easterly winds associated with the southward penetration of the STWJ (e.g., in June, the STWJ was observed over Mali for several days). From 4 to 8 km MSL, northeasterly winds are present throughout the summer season. They are linked to the African Easterly Jet (AEJ), which location changed from 5°N during the preonset period to 15°N during the mature monsoon phase (according to the ECMWF analyses). Only, the northern fringe of the AEJ reaches Tamanrasset in the months of June, July and August, when the monsoon has penetrated farthest over the continent. Finally, the harmattan is observed as an easterly flow between the surface and 4 km

MSL. The occasional presence of southwesterly winds in Tamanrasset below 4 km MSL (between the end of July and the middle of September) corresponds to the arrival of the monsoon flow over the foothills of the Ahaggar massif.

#### 4.2. Water Vapor, Clouds, and Precipitations

[22] Figure 5 presents the evolution of the water vapor mixing ratio profile obtained from radiosonde measurements, the cloud cover and the daily precipitations for 2006. Table 2 presents a summary of the cloud cover and the humidity conditions for each IOP. The evolution of the water vapor content over Tamanrasset is closely related to the wind regime. Dry conditions (water vapor mixing ratio in the SABL less than  $\sim 3$  g/kg) prevail during the whole of the winter season. Summer months are characterized by a marked increase (by a factor  $\sim 2$ ) of water vapor mixing ratio (see values during the “moisture advection” period in Table 2). The increment in water vapor results from enhanced humidity advection in the lower levels (below 4.5 km AGL, see Figure 5a) in relation with the monsoon.

**Table 2.** Evolution of Cloud Cover Over Tamanrasset in 2006<sup>a</sup>

Period	Dates	Number of Lidar Cases	Water Vapor		Cloud Cover (%)		ABL Clouds		FT Clouds	
			Mixing Ratio (g/kg)		Sky Fraction	Occurrences	Occurrences (%)	Altitude (km)	Occurrences (%)	Altitude (km)
Dust transport (IOP 1)	25 May/17 Jun	13	3.8 ( $\pm 1.0$ )	0.6 ( $\pm 0.5$ )	51 ( $\pm 23$ )	59	57	4.2 ( $\pm 0.3$ )	4	7.1 ( $\pm 0.6$ )
Dry convection (IOP 2)	25 Jun/11 Jul	17	3.3 ( $\pm 0.4$ )	0.1 ( $\pm 0.1$ )	25 ( $\pm 14$ )	20	20	4.4 ( $\pm 0.3$ )	0	–
Moisture advection (IOP 3)	7 Sep/21 Sep	16	6.3 ( $\pm 1.3$ )	0.6 ( $\pm 0.5$ )	58 ( $\pm 17$ )	61	59	3.9 ( $\pm 0.6$ )	5	8.6 ( $\pm 0.8$ )
Shallow convection (IOP 4)	5 Nov/23 Nov	20	3.6 ( $\pm 0.9$ )	0.3 ( $\pm 0.3$ )	35 ( $\pm 26$ )	26	11	2.3 ( $\pm 0.3$ )	16	7.1 ( $\pm 1.8$ )

<sup>a</sup>Mean values and standard deviations related to atmospheric variability (between brackets) for each intensive operating period (IOP) are given. Occurrences (in %) were calculated using lidar measurements during IOPs. Water vapor mixing ratio values in the ABL and FT were estimated using radiosounding data after cloud screening, averaged between 0 and 1 km AGL as well as between 7 and 8 km AGL, respectively. Cloud altitudes correspond to the cloud base height AGL. Cloud cover is expressed with respect to the portion of the sky covered by clouds (as observed by an ONM ground observer) and the occurrence of clouds (as determined by lidar in the vertical).

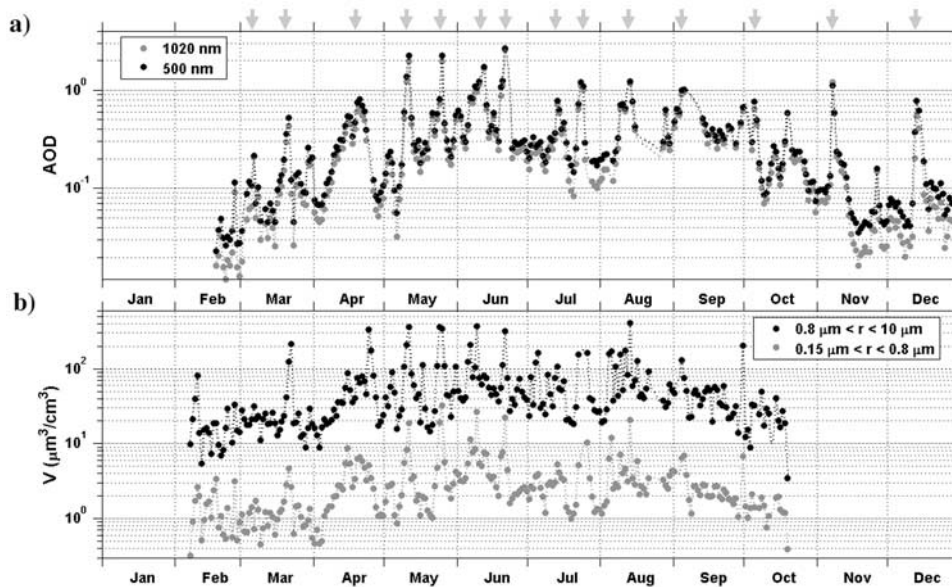


**Figure 6.** (a) Aerosol optical depth at 500 nm and 1020 nm over Tamanrasset in 2006 as obtained from Sun photometer measurements. The data were processed in the framework of the AERONET program. Cloud screened level 1.5 products are used [Holben *et al.*, 1998]. (b) Particle volume concentration at the surface (for particles in the range of radii  $0.15 \mu\text{m} < r < 0.8 \mu\text{m}$  and  $0.8 \mu\text{m} < r < 10 \mu\text{m}$ ). Particle volume concentration is estimated by integrating the number size distributions measured by the optical particle counter, considering spherical particles for number to volume conversion.

[23] Clouds were a frequent feature in Tamanrasset throughout the year (the annual mean cloud cover in 2006 is  $42 \pm 30\%$ , see Figure 5b). In the winter, the cloud cover was influenced by the STWJ with occasional midlevel and cirrus clouds around 8.5 km AGL (see Table 2), being representative of continental Saharan conditions [Dubief, 1959, 1963]. At the beginning of summer (IOP 1), clouds covered 51% of the sky on average and were present 59% of the time (see Table 2). At the end of June (IOP 2), atmospheric conditions changed radically to a much clearer atmosphere (on average 25% of cloud cover and 20% of the time), because of enhanced large-scale subsidence (see the increase in pressure in Figure 3a).

[24] In 2006, the total amount of precipitation at Tamanrasset was 59 mm (in 23 days, see Figure 5c). This is slightly above the mean values of 50 mm (in 14.5 days) observed in the period 1930–1960 [Dubief, 1963] and 48 mm in 1970–2006 (according to ONM (M. Mimouni, unpublished data, 2007)). Ten out of the 16 rain episodes which were observed from July to September were associated with southerly advection of moist monsoon air (the mean wind direction from 1.5 to 3 km AGL is from  $172^\circ \pm 82^\circ$ ).

## 5. Seasonal Evolution of the SABL Over Tamanrasset in 2006

[25] As in other regions of the world, the SABL exhibits a marked diurnal cycle. In this region, it is particularly strong [Parker *et al.*, 2005a]. One of the main factors affecting the SABL diurnal cycle is the atmospheric radiative budget. The textbook description of the different layers composing a continental planetary boundary layer (PBL) given by Stull [1988] holds for the SABL. A convective boundary layer

(CBL) develops during the daytime thanks mainly to the insolation. During the night, the radiative cooling at surface leads to the development of a nocturnal surface layer and the formation of a neutral residual layer (RL) above the stratified nocturnal surface layer.

[26] The seasonal evolution of the aerosol content, which affects the radiative budget, is first described in this section (section 5.1). The impact on the surface energy balance and the consequences on the SABL CBL development are analyzed in sections 5.2 and 5.3, respectively. Additional factors affecting the CBL growth (i.e., subsidence, moist advection, SHL position) are discussed as well.

### 5.1. Saharan Dust in the SABL

[27] Figure 6 presents the evolution in 2006 of the total column aerosol optical depth AOD (Figure 6a) and the volume concentration  $V$  of coarse ( $0.8 \mu\text{m} < r < 10 \mu\text{m}$ ) and fine ( $0.15 \mu\text{m} < r < 0.8 \mu\text{m}$ ) dust particles at the surface (Figure 6b). A brief description of the prevailing conditions and origin of each dust episode is given in the auxiliary material. Meteorological conditions and dust plume origins were analyzed using SEVIRI infrared imagery and ECMWF analyses. As indicated by the peaks in the AOD time series (marked by gray arrows in Figure 6a), 14 dust episodes occurred in Tamanrasset between March and December, lasting 3 to 14 days and 4.6 days on average (with AOD a factor 2 higher than the background value, which is evaluated as the minimum over 20 days). In 3 occasions, the AOD peaks were produced by the arrival of 2 successive dust plumes to Tamanrasset (a total of 17 dust plumes were observed). In between the peaks of 1 to 2, the AOD remained relatively low resulting in an annual mean of 0.34 at 500 nm. Given the soil characteristics in the

**Table 3.** Aerosol Content Evolution Over Tamanrasset in 2006<sup>a</sup>

Period	Dates	Number of Lidar Cases	Total Column		Surface			Aerosol Layers			
			AOD	$\dot{a}$	$N$ ( $\text{cm}^{-3}$ )	$V$ ( $\text{cm}^3/\mu\text{m}^3$ )	$N_{FC}$	$V_{CF}$	ABL: $R$ at 1 km	Occurrences (%)	Altitude (km)
Dust transport (IOP 1)	25 May/17 Jun	13	0.69 ( $\pm 0.50$ )	0.17 ( $\pm 0.08$ )	80 ( $\pm 78$ )	101 ( $\pm 97$ )	9.0 ( $\pm 1.1$ )	9.4 ( $\pm 1.8$ )	3.1 ( $\pm 1.6$ )	9	2.8 ( $\pm 0.9$ )
Dry convection (IOP 2)	15 Jun/11 Jul	17	0.27 ( $\pm 0.04$ )	0.30 ( $\pm 0.05$ )	35 ( $\pm 7$ )	69 ( $\pm 38$ )	7.8 ( $\pm 1.2$ )	10.3 ( $\pm 1.6$ )	2.1 ( $\pm 0.6$ )	5	2.8 ( $\pm 0.6$ )
Moisture advection (IOP 3)	7 Sep/21 Sep	16	0.39 ( $\pm 0.07$ )	0.20 ( $\pm 0.10$ )	31 ( $\pm 7$ )	43 ( $\pm 13$ )	9.1 ( $\pm 2.2$ )	10.4 ( $\pm 2.2$ )	2.5 ( $\pm 0.7$ )	14	2.5 ( $\pm 0.5$ )
Shallow convection (IOP 4)	5 Nov/23 Nov	20	0.18 ( $\pm 0.26$ )	0.70 ( $\pm 0.38$ )	n/a	n/a	n/a	n/a	1.5 ( $\pm 0.5$ )	4	2.1 ( $\pm 0.2$ )

<sup>a</sup> Aerosol optical depth (AOD) is provided at 500 nm. The Ångström coefficient  $\dot{a}$  is computed using AOD measurements between 440 nm and 670 nm. The surface number  $N$  and volume  $V$  concentrations of particles are given in the range of  $0.15 \mu\text{m} < r < 10 \mu\text{m}$ .  $N_{CF}$  is the same as  $V_{CF}$ , but for number concentrations. Aerosol layers indicate the presence of elevated particle layers detached from the surface, usually formed in the RL.  $R$  is the scattering ratio, i.e., the ratio of the total attenuated backscatter divided by the molecular backscatter at 1 km AGL. “n/a” stands for not available. Standard deviations related to atmospheric variability are given between brackets.

Tamanrasset area (i.e., rocky/gravel and clay-like desert soil), the major dust events were not likely to be produced locally [D’Almeida and Schültz, 1983; D’Almeida, 1986; Marticorena and Bergametti, 1995]. Moreover, observations in 2006 did not show any major dust event in Tamanrasset that originated from the closest “source region” identified in literature (i.e., about 150 km southwest of Tamanrasset, see [D’Almeida, 1986; Caquineau et al., 2002; Prospero et al., 2002]). Three mechanisms were identified to be responsible for lifting the dust observed in Tamanrasset after transport: (1) turbulence at the leading edge of cold pools associated with Mesoscale Convective Systems (MCSs) [e.g., Flamant et al., 2007] when the ITD is in the vicinity of the Ahaggar (eight such events were observed from May to September); (2) turbulence in the growing CBL mixing momentum of nocturnal low-level jets downward over source regions, such as the Bodélé depression, described by Todd et al. [2008] (six such events were observed throughout the year); and (3) interactions of the STWJ with the Atlas Mountains during the winter months (three episodes before April and after October), leading to the downslope winds propitious to the lifting of dust along the Sahara side of the Atlas Mountain chain in southern Morocco and Algeria.

[28] Throughout 2006, aerosol content and properties exhibits a marked seasonal evolution (see Table 3). During the so-called “dust transport” period (in which IOP 1 is embedded), northward propagating cold pools (associated with MCS traveling over Sahel) and low-level jets over source regions generated a succession of dust episodes. Among all IOPs, this period presented the highest dust concentration at the surface and within the SABL (as indicated by the scattering ratio  $R$  at 1 km AGL as well as the greatest AOD. After the “dry onset” (the so-called “dry convection” period, in which IOP 2 was embedded), a much clearer atmosphere (AOD and  $V$  dropped by a factor 2 or more) was observed. In the “moisture advection” period (in which IOP 3 was embedded), northward humidity transport by the WAM modified the aerosol properties over Tamanrasset, leading to higher AODs, with lower number and volume surface concentrations. In the winter “shallow convection” period (in which IOP 4 was embedded), dust concentration decreased, leading to AOD values as low as  $\sim 0.04$  (at 500 nm) by the end of November.

[29] The aerosol size distributions observed at the surface in Tamanrasset exhibited both a submicron and a coarse mode of dust particles throughout the year. Interestingly, during dust episodes, the partition between the two mode remained roughly the same (with a variability less than 10 to 15%, see Figure 6b), regardless of the season (see Table 3). The Ångström coefficient  $\dot{a}$  (which expresses the AOD spectral dependence [Ångström, 1964]) was positive and relatively low (see Table 3), indicating a small but non negligible contribution of fine particles to the total AOD. Moreover, high (low) AOD periods were characterized by lower (higher)  $\dot{a}$ , indicating a relationship between the occurrence of dust events and the dust optical properties.

[30] Furthermore, a significant correlation exists between the surface aerosol concentrations  $V$  and the total column AOD. The correlation coefficient between the AOD and the concentration for aerosol with radii in the range  $0.15 \mu\text{m} < r < 10 \mu\text{m}$  ( $0.15 \mu\text{m} < r < 0.8 \mu\text{m}$ ) is 0.73 (0.83). These

**Table 4.** Surface Energy Balance in Tamanrasset<sup>a</sup>

Period	Dates	Shortwave				Downwelling			Upwelling			
		Direct TOA	Direct	Shortwave		Global	Longwave	Total	Sensible Heat Flux	Shortwave	Longwave	Total
				Diffuse	Global							
Dust transport (IOP 1)	25 May/17 Jun	463 (±1)	148 (±84)	148 (±38)	296 (±52)	367 (±19)	663 (±36)	60 (±13)	99 (±17)	498 (±13)	668 (±31)	
Dry convection (IOP 2)	25 Jun/11 Jul	462 (±1)	257 (±33)	93 (±16)	350 (±19)	348 (±9)	698 (±16)	70 (±11)	116 (±6)	498 (±9)	686 (±16)	
After WAM onset	17 Jul/27 Jul	457 (±1)	163 (±90)	121 (±46)	284 (±48)	380 (±15)	664 (±38)	48 (±10)	93 (±15)	496 (±18)	642 (±35)	
Moisture advection (IOP 3)	7 Sep/21 Sep	408 (±7)	135 (±59)	115 (±25)	250 (±41)	372 (±13)	623 (±32)	44 (±14)	82 (±13)	493 (±13)	619 (±22)	
Shallow convection (IOP 4)	5 Nov/23 Nov	305 (±8)	175 (±38)	48 (±27)	222 (±13)	290 (±18)	512 (±14)	34 (±5)	76 (±4)	418 (±11)	529 (±12)	

<sup>a</sup>Unit is  $\text{W m}^{-2} \text{d}^{-1}$ . Shortwave radiation at the top of the atmosphere (TOA) was calculated theoretically according to *Oke* [1987]. Shortwave downwelling direct and diffuse components were evaluated over a horizontal surface unit. Ground-based latent heat fluxes ( $<5\%$  of sensible heat flux according to ECMWF analysis) are not considered in the analysis (not measured in Tamanrasset). The upwelling infrared and visible fluxes were estimated as  $\varepsilon\sigma T_{\text{surface}}^4$  and  $\omega_r L_r^{-1} + \omega_f L_f^{-1}$ , respectively ( $\varepsilon$  being the surface emissivity,  $\sigma$  the Stefan-Boltzmann constant,  $\omega$  the surface albedo,  $L^{-1}$  the downwelling visible flux and the indexes  $r$  and  $f$  for the direct and diffuse components). MODIS land products with a 1-km horizontal resolution (<http://edc.daac.usgs.gov/dataproducts.asp>) were used to estimate the surface emissivity  $\varepsilon$  (0.97) and surface albedo  $\omega$  (from 0.32 to 0.34).

correlations suggest vertical mixing through the SABL and coupling with the surface during daytime. After being lifted from the ground in source regions, dust plumes over the Sahara are essentially transported within the SABL. On the contrary, when Saharan dust layers are transported beyond the Sahara, they typically rise over the cooler and moister air encountered near the surface and form an elevated layer decoupled from the surface, referred to as the Saharan Aerosol Layer or Saharan Air Layer in literature [e.g., *Karyampudi and Carlson*, 1988]. This occurs over the Atlantic Ocean, particularly in the summer season [e.g., *Reid et al.*, 2002; *Tanré et al.*, 2003], the sub-Saharan regions during the mature monsoon period [e.g., *Parker et al.*, 2005b] and the Mediterranean [e.g., *Papayannis et al.*, 2004].

## 5.2. Surface Energy Balance

[31] The annual evolution of the surface energy fluxes in Tamanrasset and the interactions with dust content and cloud cover were investigated (see Table 4). Sensible heat flux and downwelling visible and infrared fluxes were observed directly. Upwelling visible and infrared components were estimated using MODIS retrievals of the surface albedo and emissivity (see section 2.3). The coherence of the measurements was checked through a verification of the surface energy fluxes closure, using measured (i.e., downwelling radiative and sensible heat fluxes) and calculated (i.e., upwelling radiative) fluxes. The difference between the total fluxes for the four IOPs was less than 2% (within the daily variability of the fluxes), independently of the differences in the meteorological conditions (i.e., dust content, cloud cover, humidity). The discrepancy was higher (4%) for the period after the WAM onset, probably caused by an increase in the latent heat flux (not available) after rainfall episodes.

[32] During both the “dust transport” and “after WAM onset” periods, atmospheric radiative forcing due to aerosols and clouds induced a 50–50 partition between direct and diffuse visible fluxes. A significant absorption of global insolation (36% and 38%, respectively) was also observed, a larger proportion than during the “dry convection” period (24%). During dust events, aerosols absorbed typically 5% to 20% of solar radiation. This is estimated for single particle-light interaction as  $\sim \exp((\omega_0 - 1) \text{AOD})$  at 500 nm,  $\omega_0$  being the single scattering albedo retrieved with the Sun photometer almucantar algorithm for spheroid particles, according to *Dubovik and King* [2000] and *Dubovik et al.* [2002]. In the winter (“shallow convection” period), clear sky conditions with very low aerosol loads and cloud covers resulted in an elevated surface insolation, relatively close to the solar radiation at the top of the atmosphere (TOA). During this season, aerosols only absorbed  $\sim 0.5\%$  of the solar radiation. The seasonal evolution of aerosol content and cloud cover reduced the differences between winter and summer surface insulations, i.e., the minimum (maximum) of atmospheric transmission occurred in the summer (winter), when TOA solar radiation is maximum (minimum). Maximum surface insolation occurred in April, as the TOA insolation was relatively high while aerosol load, humidity and cloud cover remained relatively low.

[33] Downwelling infrared or terrestrial flux displayed a maximum during the wet season (end of July, August and

**Table 5.** Evolution in 2006 of Convective Development of the SABL in Tamanrasset and Other Related Variables<sup>a</sup>

Period	Dates	Number of Lidar Cases	CBL Height (km)		SABL Height (km)		Maximum Sensible Heat Flux ( $W m^{-2}$ )	Surface-Air Temperature Gradient ( $^{\circ}C$ )	Subsidence (m/h)
			1200 UTC	1800 UTC	Mean	Maximum			
Dust transport (IOP 1)	25 May/17 Jun	13	3.9 ( $\pm 0.8$ )	4.4 ( $\pm 0.5$ )	3.9 ( $\pm 0.8$ )	4.1 ( $\pm 0.7$ )	207 ( $\pm 46$ )	14.4 ( $\pm 3.4$ )	-8
Dry convection (IOP 2)	25 Jun/11 Jul	17	3.7 ( $\pm 1.1$ )	4.7 ( $\pm 0.5$ )	4.1 ( $\pm 1.0$ )	4.5 ( $\pm 0.8$ )	247 ( $\pm 41$ )	14.8 ( $\pm 2.6$ )	-43
After WAM onset	17 Jul/27 Jul	0	3.4 ( $\pm 1.0$ )	3.8 ( $\pm 0.7$ )	n/a	n/a	172 ( $\pm 37$ )	12.7 ( $\pm 3.2$ )	-19
Moisture advection (IOP 3)	7 Sep/21 Sep	16	3.2 ( $\pm 1.0$ )	2.9 (1.0)	3.6 ( $\pm 0.6$ )	3.8 ( $\pm 0.5$ )	187 ( $\pm 55$ )	14.2 ( $\pm 1.5$ )	-6
Shallow convection (IOP 4)	5 Nov/23 Nov	20	1.6 ( $\pm 0.6$ )	n/a	1.9 ( $\pm 0.6$ )	2.2 ( $\pm 0.4$ )	138 ( $\pm 23$ )	11.9 ( $\pm 1.5$ )	-41

<sup>a</sup>The CBL height  $h_{CBL}$  was the lowest critical inversion according to *Heffler* [1980], using as criteria  $\Delta\theta/\Delta z \geq 0.0025 K/m$  and  $\theta_{top} - \theta_{base} \geq 1 K$ . The daily mean and maximum SABL heights were determined by the lidar signal gradient (in attenuated backscatter at 532 nm) between the molecular return and the aerosol layers identified as the top of the SABL and the cloud base for cloud-topped SABLs. The daily maximum sensible heat fluxes correspond to the mean values between 1100 UTC and 1300 UTC. The surface-air temperature gradient was calculated as the difference between the daily maximum temperature of the surface (measured 1 cm above the ground) and the air (measured at 2 m above the ground). Large-scale subsidence was estimated using ECMWF analysis at 400 hPa ( $\sim 7.5$  km MSL) and averaged over each period.

September), in conjunction with an increase in cloud cover and moisture at lower levels. The mean seasonal variability was  $\sim 23\%$  for the telluric flux, whereas it was  $\sim 60\%$  for the solar flux. Furthermore, the greatest seasonal relative variability ( $>100\%$ ) was exhibited by the turbulent sensible heat flux, between the maximum and minimum of surface insolation in the “dry convection” and “shallow convection” periods. Moreover, the sensible heat flux in the “after WAM onset” period was significantly affected by a reduction in the mean surface-air temperature gradient, with similar surface insolation but lower sensible heat flux than in the “dust transport” period (see Table 5).

### 5.3. Convective Development of the SABL

[34] Figure 7 shows the evolution in 2006 of the CBL height  $h_{CBL}$  estimated from the 1200 UTC and 1800 UTC radiosoundings and daily maximum sensible heat flux  $H_S^{MAX}$ . Table 5 presents numerical values of these and other complementary variables (i.e., SABL height, large-scale subsidence, surface-air temperature difference) for the four IOPs and the “after WAM onset” period. In 2006, the CBL evolved from a 1.5 to 2 km shallow layer in winter to a 5 to 6 km deep layer in the summer season. The seasonal evolution of  $h_{CBL}$  was influenced both by the surface energy balance and the prevailing meteorological conditions (e.g., subsidence, cool/moist or hot/dry air advection). The pronounced subsidence in the “dry convection” period delayed the CBL development in the morning (see the difference in  $h_{CBL}$  between 1200 UTC and 1800 UTC from 15 June to 10 July). In turn, subsidence-induced clear sky conditions resulted in stronger solar insolation and enhanced the CBL development in the late afternoon (see  $h_{CBL}$  at 1800 UTC from 20 June to 10 July). By the end of this period, the fully developed CBL were the deepest observed for the year 2006. Moreover, these fully developed CBLs systematically reached the altitude at which most elevated dust layers (aerosol layers in Table 3) were observed earlier in the morning. As a result, the dust layers located in the RL were systematically mixed into the developing CBL. Hence, a single, deep dust layer was observed within the SABL by the end of the day (e.g., 11 June in section 6.1); in conjunction with the fact that dust plumes were mostly transported within the SABL (see section 5.1). These deep, well mixed dust layers have previously been observed over the Atlantic ocean [e.g., *Reid et al.*, 2002; *Tanré et al.*, 2003].

[35] The diurnal evolution of  $H_S^{MAX}$  (Figure 7b) exhibits a large variability on a daily basis, sometimes up to 100% on consecutive days. The ratio between the annual maximum and annual minimum values of the 10-day averaged  $\langle H_S^{MAX} \rangle$  is  $\sim 2.5$  (Figure 7b), whereas it is only  $\sim 1.5$  for visible fluxes. Moreover, sudden changes (up to 50%) in  $\langle H_S^{MAX} \rangle$  are observed during the WAM onset phase period (June and July). The sensible heat flux  $\langle H_S^{MAX} \rangle$  in Tamanrasset increases by  $59 W m^{-2}$  between 15 June and 5 July and then decreased by  $115 W m^{-2}$  ( $\sim 40\%$ ) between 15 and 27 June. This reduction in  $\langle H_S^{MAX} \rangle$  coincides with a drop in surface pressure (see Figure 3a) that marked the influence of the SHL in Tamanrasset (see section 4). This concomitance was also pointed out by *Ramel et al.* [2006]. They identified a marked reduction of  $\langle H_S^{MAX} \rangle$  over southern Sahara ( $15^{\circ}W-0^{\circ}E$ ,  $20-25^{\circ}N$ ) as a triggering factor for the north-

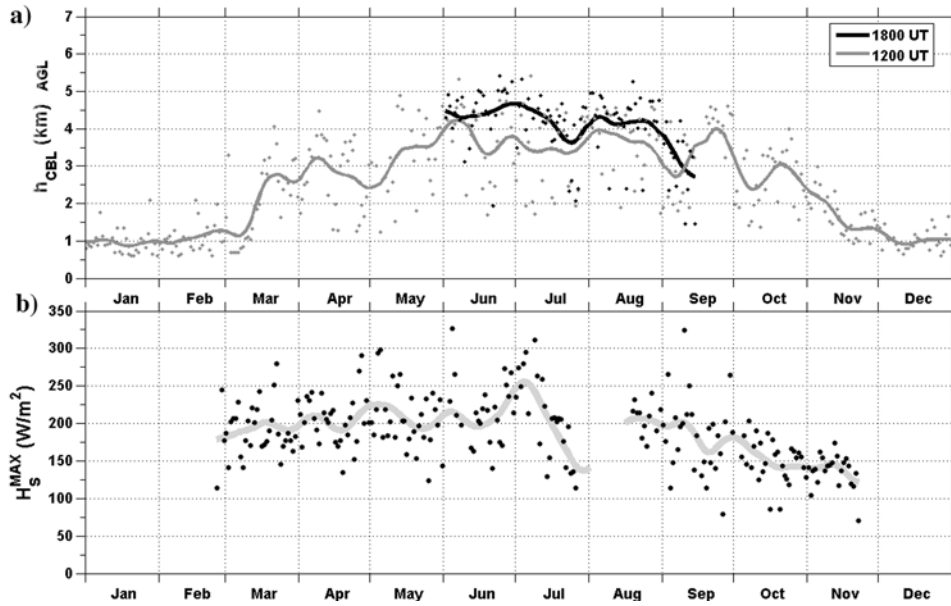


**Figure 7.** (a) Convective boundary layer height  $h_{CBL}$  determined from the 1200 and 1800 UTC soundings in Tamanrasset. (b) Daily maximum value of the turbulent sensible heat flux  $H_s^{MAX}$  (averaged between 1100 UTC and 1300 UTC). Daily values are indicated by dots while low-pass filtered data (10-day sliding window) are given by solid gray lines.

ward displacement of the SHL/WAM system (i.e., the monsoon onset).

[36] An additional factor affecting the SABL development in the summer was the location and strength of the SHL. As the SHL influence in Tamanrasset was strongest (i.e.,  $-4$  hPa in surface pressure) from 1 to 15 August (see Figure 3a), the vertical extent of the SABL increased in average by  $\sim 500$  m (see  $h_{CBL}$  at 1800 UTC). Then,  $h_{CBL}$  reached a second relative annual maximum, while the daily maximum surface temperature remained almost constant (see Figure 3b). Once the SHL influence disappeared (around 15 September), the SABL depth decreased by  $\sim 1$  km, although similar  $\langle H_s^{MAX} \rangle$  values were observed both on 15 August and 15 September. This enhancement of the depth of the SABL in the presence of the SHL is consistent with the fact that strong vertical motion is generally observed within the SHL region as the result of low-level convergence.

## 6. Vertical Structure and Diurnal Cycle of the SABL

[37] In Tamanrasset, the vertical structure and the diurnal cycle of the SABL were monitored during the four IOPs described in section 3. SABL observations were primarily based on a synergy between ground-based and spaceborne lidar, balloon-borne (radiosonde) profiling and additional ancillary data. In sections 6.1 to 6.4, one case study representative of each of the four IOPs is presented.

### 6.1. Saharan Dust Transport and Dry Convection

[38] During the first IOP (25 May to 17 June), atmospheric conditions were characterized by high aerosol concentrations in a deep SABL (see Table 5). Occasional episodes of Saharan dust occurred as the result of transport

of dust plumes originating from major source regions (as on 11 June).

[39] Figure 8 presents MiniLidar derived time series of total attenuated backscatter coefficient profiles (at 532 nm) on 11 June. Lidar profiles time series enable the identification of cloud layers (strong return signal and temporal variability of the order of  $\sim 1$  min), aerosol layers (strong return signal, generally weaker than that associated with clouds, and a temporal variability of the order of  $\sim 10$  min) and clear-air regions (no scatterers other than molecules, where the lidar signal decreases smoothly as a function of increasing altitude). Lidar time series were calibrated in a “particle-free” region (blue arrow on the left of Figure 8a) using molecular backscatter coefficient  $\beta_m$  (in  $sr^{-1} m^{-1}$ ), calculated using the following equation [Measures, 1984]

$$\beta_m(z) \cong 1.38 \left( \frac{550}{\lambda} \right)^{4.09} \left( \frac{p(z)288}{1013T(z)} \right) \cdot 10^{-6} \quad (1)$$

where  $z$  is the altitude (in km),  $\lambda$  is the wavelength of operation of the lidar (in nm),  $p$  is pressure (in hPa) and  $T$  is temperature (in K), the latter two variables being derived from radiosonde measurements at 0600 UTC. The calibration coefficient obtained for the “particle-free” region is extrapolated to the rest of the time series. At noon, the signal-to-noise ratio (SNR) of the lidar profiles was reduced because of the increase of the spurious signal induced by solar insolation (the lidar telescope pointing almost in the direction of the Sun). Noise becomes apparent at altitudes higher than 7 km AGL and saturation of the detectors occurs at 1130 UTC (Figure 8a). The lidar was pointing at  $3^\circ$  off the zenith to reduce this effect. The total backscatter profiles  $\beta(z)$  of Figures 8c and 8d (and Figures 10–12) are derived using a standard backscatter lidar inversion technique [Fernald et al., 1972; Fernald, 1984] with a

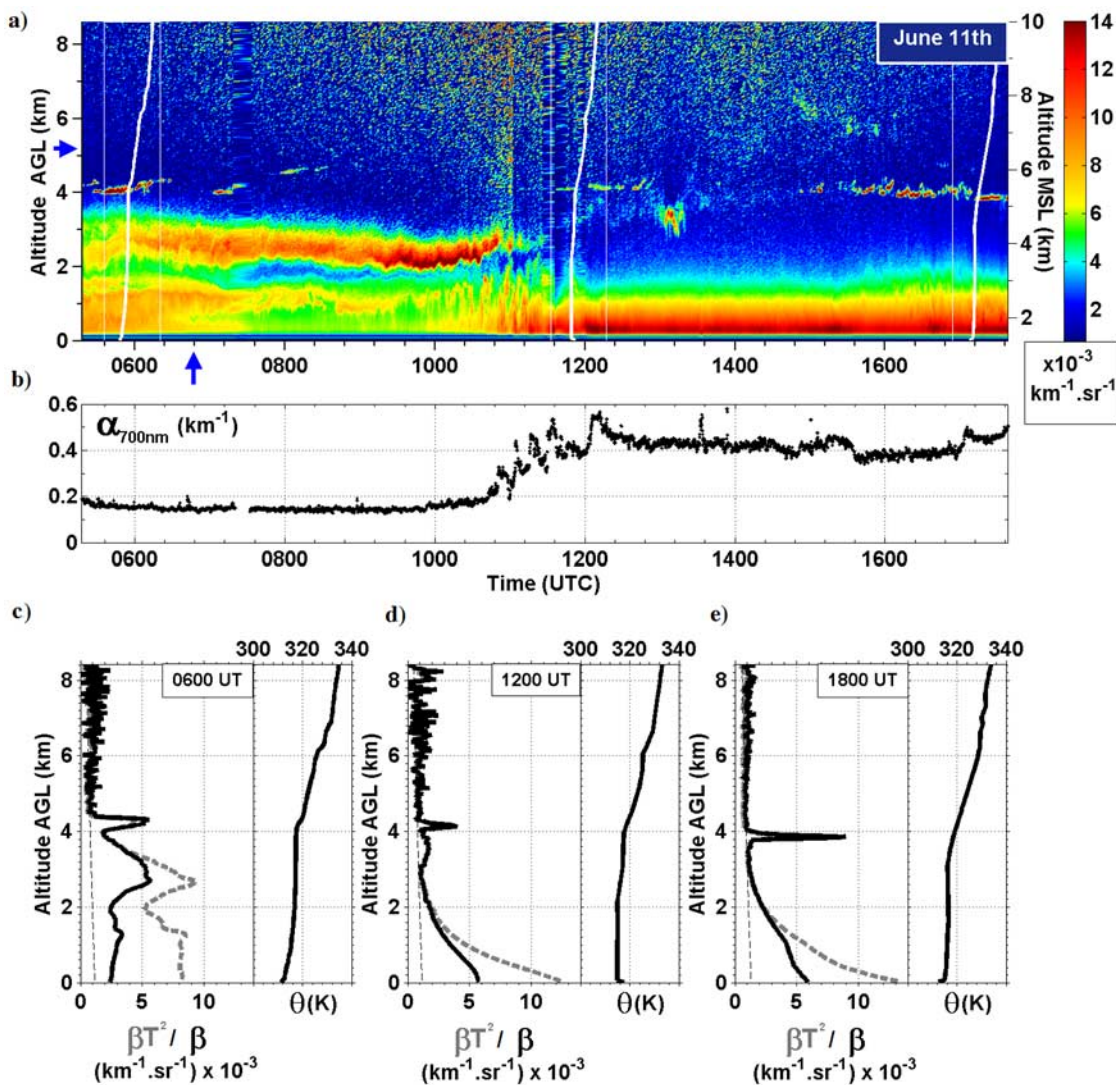


**Figure 8.** (a) MiniLidar derived total attenuated backscatter coefficient profiles at 532 nm on 11 June 2006. Altitudes are AGL (left axis) and MSL (right axis) and time is UTC (local time = UTC + 1 h). Lidar profiles were calibrated in a particle-free region of the troposphere (indicated by the blue arrow). The potential temperature profiles from radiosoundings made at 0600 UTC, 1200 UTC, and 1800 UTC are superimposed (white solid lines). Each potential temperature profile is plotted between 300 K and 340 K. (b) Surface aerosol scattering coefficient at 700 nm. Individual MiniLidar profiles (30 min averages) at (c) 0600 UTC, (d) 1200 UTC, and (e) 1800 UTC, respectively. The dashed gray lines, the solid black lines, and the thin dashed lines are the attenuated backscatter profiles  $\beta T^2(z)$ , the total backscatter profiles  $\beta(z)$ , and the molecular backscatter profiles  $\beta_m(z)$ , respectively. The attenuated profiles were extrapolated from 150 m AGL down to the surface (in the range of incomplete overlap between the emitter divergence and detection field of view).

constant particle backscatter-to-extinction ratio of  $0.016 \text{ sr}^{-1}$ , representative of dust particles [Kaufman *et al.*, 2003].

[40] In the early morning of 11 June (0600 UTC), the layer of enhanced reflectivity between the surface and 1.2 km AGL corresponds to the stratified SBL (formed during the night). The horizontal visibility associated with this layer was on the order of 15 km (from ONM observer). Above this layer and up to 4.1 km AGL, a nearly neutrally stratified RL from the previous day is observed. A temperature inversion located at 4.1 km AGL (as seen in the sounding data) as well as enhanced reflectivity revealing the presence of thin clouds (as seen in the lidar data), marked

the top of the RL. The enhanced reflectivity observed in the RL between 2.6 and 3 km AGL was related to a dust transport episode from a remote location. This layer could be tracked in the lidar data until approximately 1230 UTC. The CBL was observed to develop from 0700 UTC. Within the CBL, thermals could be observed. As the CBL continued to grow, they eventually reached an altitude of 2.1 km AGL at 1100 UTC. At this stage, the particle layer within the RL was eroded by the growing CBL. The CBL was fully developed at 1500 UTC, extending up to 4.2 km AGL, its depth remaining constant until the evening hours. Thin

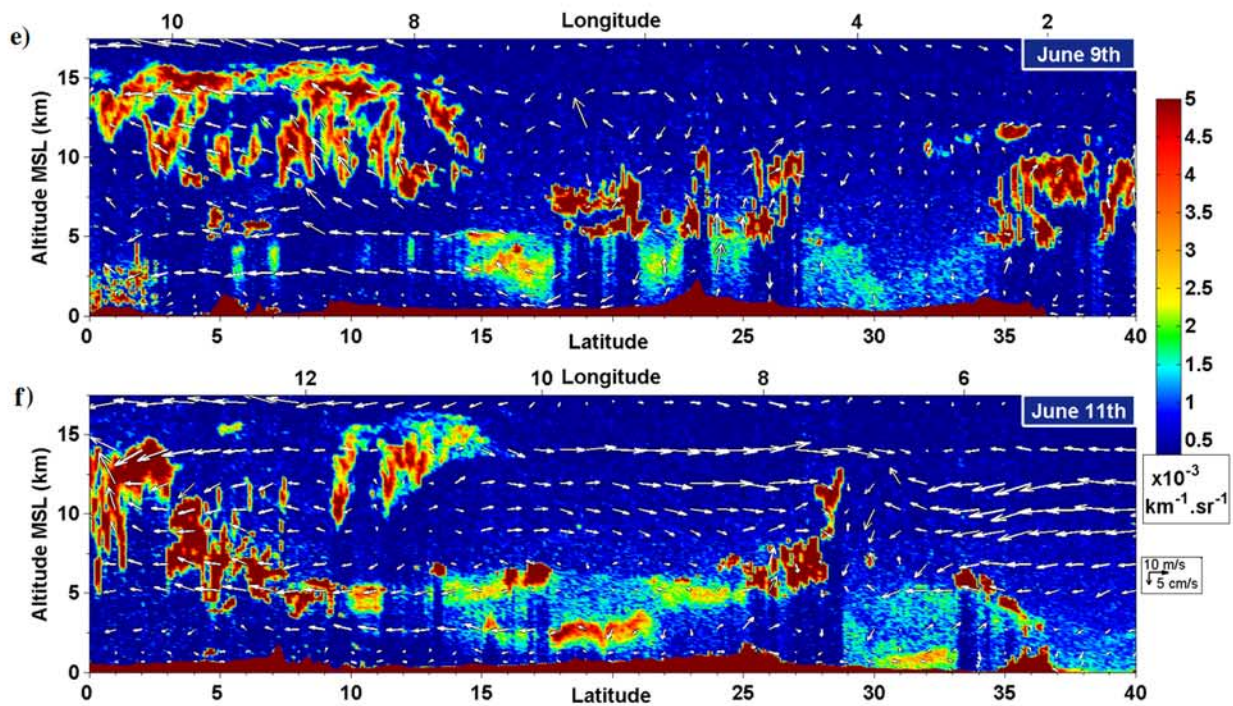
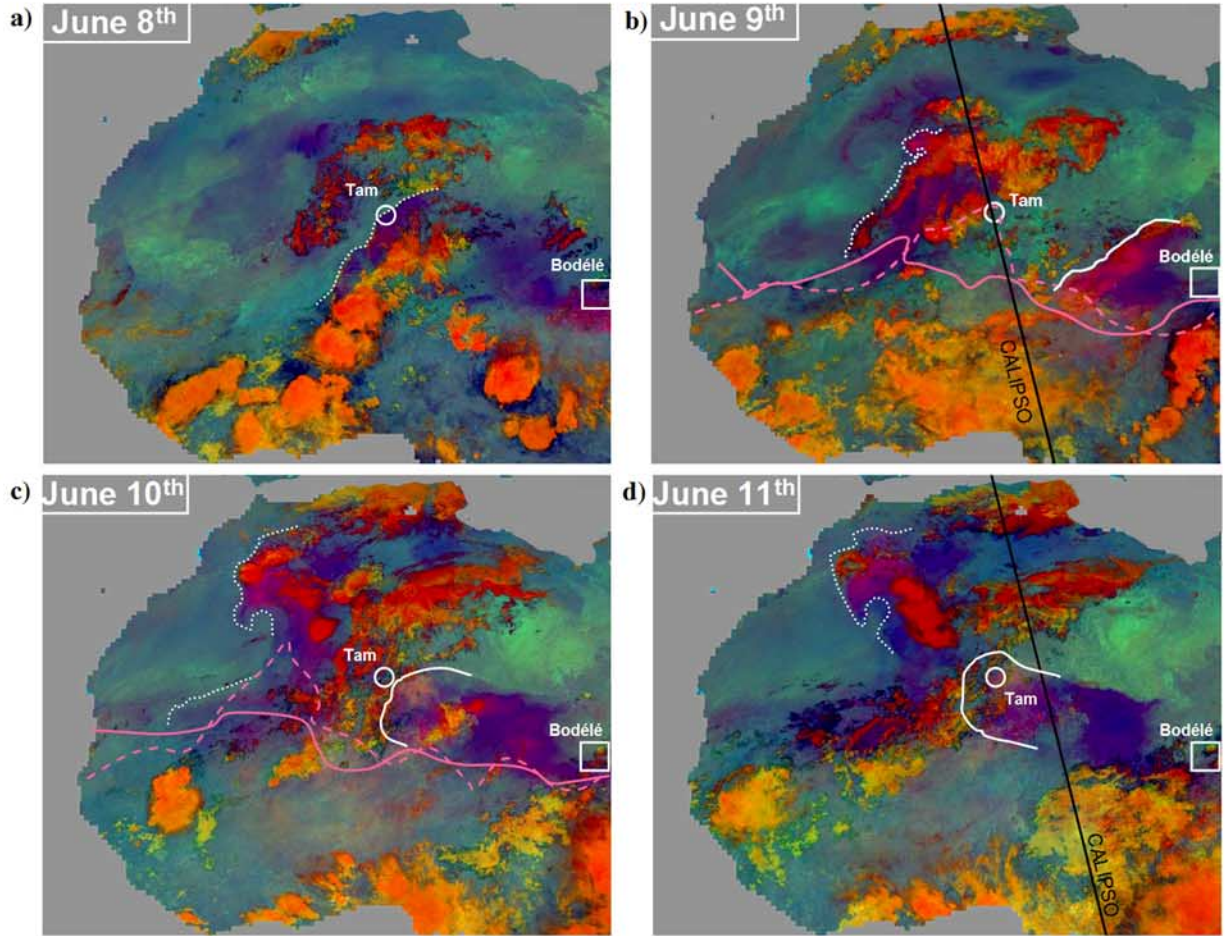


Figure 9

clouds at the top of the SABL were also observed by lidar during that period.

[41] During the morning, the scattering coefficient measured at the surface, which is proportional to the concentration and the scattering cross section of dust particles, remained nearly constant until 1030 UTC (Figure 8b). During that period, the  $\beta$  profile (Figure 8c) exhibited a well defined elevated dust layer, above a less dense layer reaching the surface. Clouds were present at the top of the RL (sharp backscatter peak at 4.1 km AGL).

[42] Shortly after 1030 UTC the scattering coefficient increased until 1230 UTC (Figure 8b). At 1300 UTC, it reached values a factor of 2.3 higher than in the morning while the CBL top reached an altitude of 3.1 km AGL. The entrainment processes at the top of the CBL is responsible for the downward mixing of the dust layer at 2.6 km AGL into the growing CBL. This led to a reduction of the horizontal visibility at the surface (from 15 to 4 km) and an enhancement of the lidar reflectivity in the CBL (Figure 8a). The  $\beta$  profile at 1200 UTC (Figure 8d) exhibited a thin layer at the RL top (thinner than at 0600 UTC) as well as a layer of enhanced reflectivity between 3 and 4 km AGL. The elevated layer corresponded to the top part of the transported dust layer, the lower part of the layer (as seen at 0600 UTC, Figure 8c) having been mixed into the CBL. This layer was no longer observed at 1800 UTC (see Figure 8e, note a thin cloud layer at the SABL top).

[43] The total backscatter profiles acquired in the afternoon (see Figures 8d and 8e) showed that dust particles were nonuniformly distributed in the vertical in the CBL, with higher backscatter values near the surface. Note that the full lidar overlap is reached at 150 m AGL. Most of the observations made with the ground-based system during the different IOPs, but also retrieved from the CALIPSO lidar in the vicinity of Tamanrasset, consistently showed such a nonuniform vertical distribution, decreasing with altitude. This behavior was verified for backscatter profiles derived for a variety of particle backscatter-to-extinction ratios ( $0.016 \text{ sr}^{-1} \pm 50\%$ ) and considering multiple scattering effects [Ackermann *et al.*, 1999], and is considered to be a robust feature. These observations are also supported by the theoretical work of Xiao and Taylor [2002]. Considering an equilibrium state between vertical turbulent diffusion and gravitation settling, they suggest that the number concentration of suspended particles above a surface decreases with increasing height, according to a power law. The

number concentration that decreases with height is greater for larger particle settling velocities, and is particularly important for coarse particles (i.e.,  $r > 6 \mu\text{m}$ ).

[44] The origin and transport patterns of the dust plumes that reached Tamanrasset on 11 June were investigated for the 8 to 11 June period by means of SEVIRI infrared images (Figures 9a–9d), wind fields from ECMWF analysis and CALIPSO vertical attenuated backscatter coefficient profiles (Figures 9e and 9f). On 8 June, a MCS (appearing in orange in Figure 9a) developed southeast of Tamanrasset and traveled toward the Ahaggar. A dust front progressed northwestward ahead of the MCS (dust appears in magenta in Figure 9a, the leading edge of the dust front is marked by the dashed line). The dust was lifted at the leading edge of the cold pool generated by the MCS, as frequently observed in this region [e.g., Knippertz *et al.*, 2007; Flamant *et al.*, 2007]. The following days, the dust plume progressed in two directions (westward and northwestward). On 8 June, a dust plume was also observed to the northwest of Bodélé depression (Figure 9a) known to be a major dust source [Prospero *et al.*, 2002; Washington *et al.*, 2006]. The following days, the second dust layer was transported westward and to the north of the ITD (dashed and solid lines in Figures 9b and 9c) and arrived in Tamanrasset on 11 June (Figure 9d).

[45] The vertical distribution of the dust plume was documented by the CALIOP lidar close to Tamanrasset on 9 June (Figure 9e) and southeast of Tamanrasset on 11 June (Figure 9f). On 9 June, dust was observed in the SABL between  $14^\circ\text{N}$  and  $31^\circ\text{N}$ . The dust to the north of Tamanrasset corresponded to that lifted at the leading edge of the cold pool on 8 June. South of Tamanrasset, the dust was originating from the Bodélé depression region and was transported to the north of the ITD. CALIOP data also suggest that the dust was mixed throughout the depth of the SABL. On 11 June, the dust plume from Bodélé was confined below an altitude of 3.5 km MSL and was observed between  $17.5^\circ\text{N}$  and  $22.5^\circ\text{N}$ , although the SABL extended up to 6 km MSL. Ground based observations made in Tamanrasset (Figure 8) suggest that the dust plume lifted up to 4.5 km MSL (3.1 km AGL) once being transported over the Ahaggar.

## 6.2. Strong Dry Convection and SABL Deepening

[46] During the second IOP, the aerosol content in the SABL as well as the cloud cover over Tamanrasset

**Figure 9.** SEVIRI-derived false color images of the West Africa on (a) 8 June at 2200 UTC, (b) 9 June at 2000 UTC, (c) 10 June at 1800 UTC, and (d) 11 June at 0200 UTC. Aerosols, clouds, and land surface are identified by the purple, orange, and green colors, respectively. The open circle and the square indicate Tamanrasset and Bodélé depression ( $18^\circ\text{N}$   $17^\circ\text{E}$ ) in Chad, respectively. The white dotted lines indicate the position of dust fronts associated with the leading edges of cold pools. The thick white lines indicate the position of the dust fronts associated with plumes from the Bodélé depression. The black solid lines in Figures 9b and 9d indicate the CALIPSO track on 9 and 11 June. The pink dashed (solid) lines in Figures 9b and 9c indicate the position of the ITD at 0600 UTC (1800 UTC) as derived from ECMWF analyses. CALIOP measurements at 532 nm along the tracks shown in Figures 9b and 9d for (e) 9 June (1309 UTC) and (f) 11 June (1252 UTC). CALIPSO passed 15 km to the west (325 km to the east) of Tamanrasset on 9 June (11 June). The CALIOP lidar data were processed with a 60-m resolution on the vertical and a 12-km resolution on the horizontal. CALIOP backscatter profiles have been normalized at 25 km of altitude by NASA Langley Atmospheric Science Data Center (<http://eosweb.larc.nasa.gov>). The outline of the topography appears in dark red. ECMWF analyses derived wind fields projected onto the satellite trajectory are superimposed to the CALIOP measurements. A scale factor of 50 was used between the vertical and horizontal wind components.

decreased significantly (see Table 3). These conditions lead to the formation of deeper SABLs with respect to IOP 1, as illustrated by the case of 25 June (Figure 10). In the early morning, a deep and slightly stratified ( $\sim 0.5$  K/km) RL was observed up to 5 km AGL. Convective plumes near the surface first appeared around 0800 UTC leading to rapidly growing CBL, deepening at a rate of  $\sim 1$  km/h, until its top reached 5.6 km AGL at 1300 UTC (as indicated by the cloud base in the lidar data). As already observed during IOP 1, lidar-derived backscatter profiles in the SABL were sloping with height (Figures 10c–10e).

[47] After 1430 UTC, a solid cloud deck formed at the top of the SABL. The cloudy layer was embedded in the CBL. It deepened in the late afternoon and reached an altitude of 7.4 km MSL (the cloud top is indicated by the relative humidity profile at 1800 UTC and CALIOP transect at 1304 UTC, Figure 10g). These clouds did not have the signature of fair weather cumuli in the lidar data (generally characterized by a flat base). The ragged lidar signature associated with the cloud deck is thought to be caused by the alternation of updrafts in the SABL and downdrafts associated with virga (this was corroborated by data from the wide-angle camera). These downdrafts were likely induced by radiative cooling at the cloud top.

[48] Dusty updrafts were also observed in some instances in the lidar data in the form of enhanced reflectivity columns within the developing CBL (see Figure 10a between 1200 and 1300 UTC for example). These features were connected to the surface as evidenced by the occurrence of maxima of surface scattering coefficient (Figure 10b). Furthermore, the friction velocity  $u^*$  was enhanced up to 60–80 cm/s when such updrafts occurred (Figure 10c). According to *Shao* [2000], particles with radius  $r$  greater than  $\sim 2$   $\mu\text{m}$  are likely lifted up beyond this threshold and are sufficiently light for remaining in suspension. Nearly 30% (in volume) of the aerosols sampled with the optical particle counter were greater than this size, thereby explaining the occurrence of such dusty thermals.

[49] The CALIOP data (at 1304 UTC) evidenced that the depth of the PBL over West Africa was increasing with latitude, from 4.5 km at the Guinean coast to 7 km in the vicinity of the Atlas Mountain (Figure 10g). Clouds were observed to form at the top of the SABL above the Ahaggar and the Atlas. The SABL top altitude derived from CALIOP data closest to Tamanrasset (distant from 15 km), matched its MiniLidar derived counterpart within  $\pm 60$  m.

### 6.3. Moisture Advection

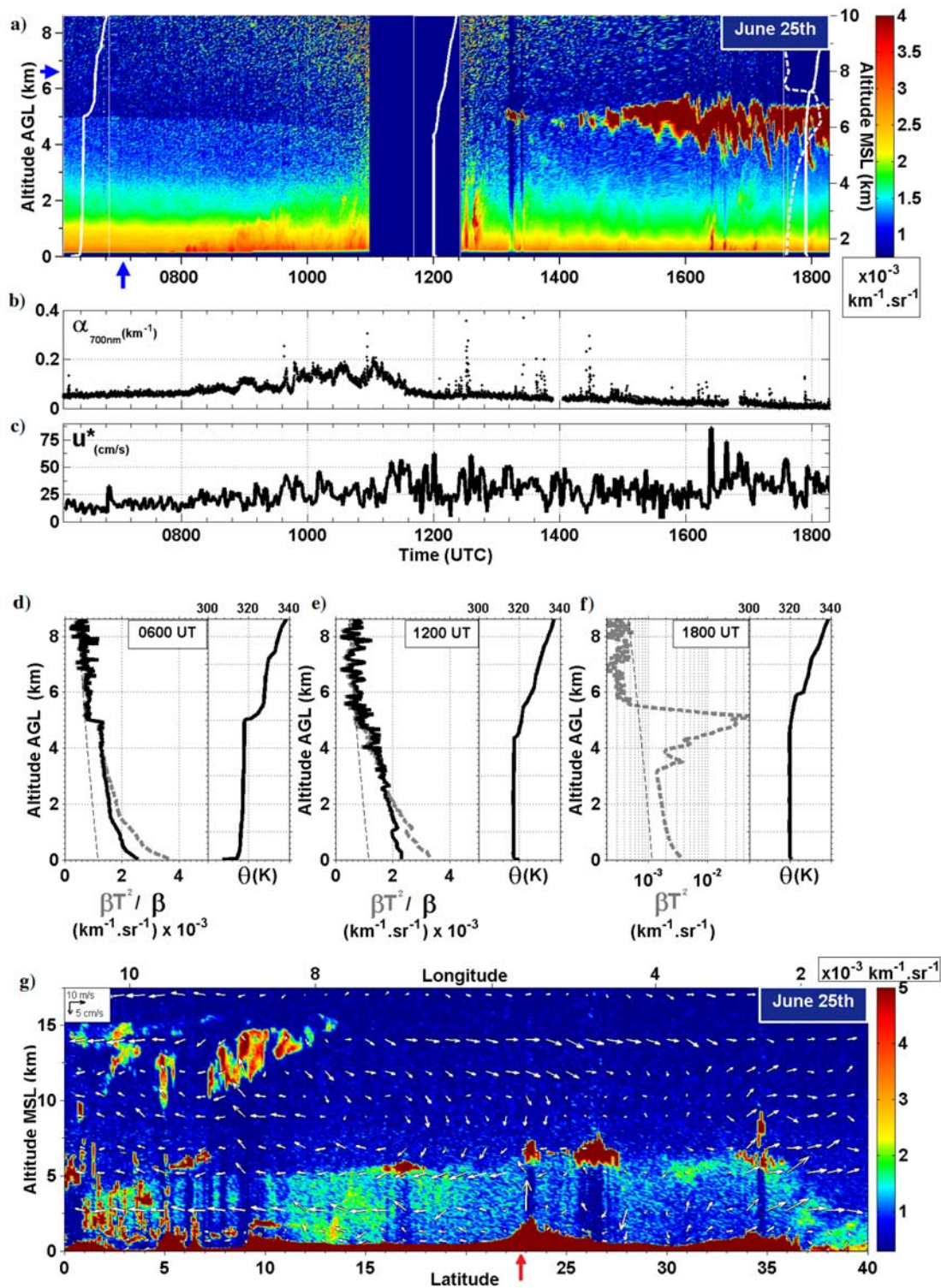
[50] The humid season in Tamanrasset was fully installed during the month of September (see Figure 5). The formation of clouds at the top of a well developed SABL was a recurrent feature (see Table 2). These clouds occasionally produced precipitation but this precipitation rarely reached the ground (i.e., virga), as on 18 and 19 September (Figure 11a). On these days, a stratocumulus cloud deck was observed from 1200 UTC on 18 September to 1800 UTC on 19 September, between 3.6 and 5.9 km AGL (i.e., between two temperature inversions, see Figure 11a). On 18 September, the condensation level was observed to be roughly 1.3 km lower than on 25 June (see

Figure 10a), which limited the CBL growth. This was related to the monsoon-related moisture advection leading to an increase in the water vapor ratio in the SABL by a factor of 2 (see Table 2), while temperatures in the SABL were quite similar to those observed during IOP 2. Cloud structures were characterized by a well defined base during the evening and wet downdrafts during the daytime (between 1100 and 1800 UTC on 18 September and between 0700 and 1500 UTC on 19 September). Cloud downdrafts indicated the destabilization of the cloud base in the presence of convective activity within the CBL (also suggested by rapid oscillations in the lidar signal near the surface). The occurrence of opaque clouds in backscatter lidar profiles produced very strong returns (50 times stronger than aerosols in the SABL) and lead to a complete extinction of the lidar signal above the cloud tops (see Figures 11c and 11d). Clouds dissipated in the evening (around 1800 UTC) of 19 September and formed again the following day.

[51] According to the CALIOP data (Figure 11e), the regional structure of the SABL was less homogenous than during the summer (see Figure 10g). It was much more shallow ( $< 2$  km deep) in the northern Sahara (north of  $28^\circ\text{N}$ ). The cloudy situation observed in Tamanrasset covered most of the Ahaggar plateau. South of the Sahara, an anvil-shaped cloud around  $10^\circ\text{N}$  marked the ITCZ. At 16 km MSL, the descending branch of the Hadley cell reached  $17^\circ\text{N}$ .

### 6.4. Shallow Convection and Clear Sky Conditions

[52] During the winter season, meteorological conditions changed drastically. Dry and nearly dust free conditions (see Tables 2 and 3) prevailed and were maintained over most of the period from mid-November 2006 to end of January 2007 (according to ONM observations). Cirrus clouds in the upper troposphere, large-scale subsidence and weak dry convection in the SABL also characterized the winter season. The 21–22 November data presented in this section (Figure 12) is representative of these conditions. A weak aerosol loading (close to the detection limit of the MiniLidar) was observed during two consecutive diurnal cycles of a rather shallow SABL (see Figure 12a). During the daytime, the CBL top reached a maximum altitude of 2 km AGL. During the night, the RL top steadily subsided after sunset at a mean rate of  $130$   $\text{m h}^{-1}$ , until the RL was as shallow as 700 m on the following morning. Further evidence of subsidence is given by the apparent downward movement of the aerosol layer observed in the free troposphere (seen in Figure 12a, from 1.8 to 2.8 km AGL, on 22 November from 0000 UTC to 1000 UTC). ECMWF analyses derived wind fields over the Sahara suggest that the descending branch of the Hadley cell was located at  $27^\circ\text{N}$ , thereby affecting the Ahaggar. Dusty thermals could be identified within the CBL between 0800 UTC and 1700 UTC (see Figures 12a and 12c). The signature of freshly lifted particles in the lidar data was particularly strong because of the contrast with a weak background aerosol concentration. The possible influence of humidity on particle optical properties was negligible as relative humidity remained below 30% [*Hänel*, 1976; *Rood et al.*, 1987]. Backscatter profiles in Figures 12b–12d evidence the weak dust concentration in the SABL with



**Figure 10.** (a) MiniLidar derived total attenuated backscatter coefficient profiles at 532 nm on 25 June 2006. Lidar profiles were calibrated in a particle-free region of the troposphere (indicated by the blue arrow). The potential temperature (relative humidity) profiles from radiosoundings made at 0600 UTC, 1200 UTC, and 1800 UTC are superimposed (white solid and dashed lines, respectively). Each potential temperature (relative humidity) profile is plotted between 300 K and 340 K (0 and 100%). (b) Surface aerosol scattering coefficient at 700 nm. (c) Friction velocity measured at 10 m from the surface by the sonic anemometer. Individual MiniLidar profiles (30 min averages) at (d) 0600 UTC, (e) 1200 UTC, and (f) 1800 UTC. The meaning of the solid and dashed lines is the same as in Figure 8. (g) CALIOP measurements over West Africa at 1304 UTC on 25 June. See Figure 8 for a description of the CALIOP resolution as well as the meaning of the arrows.

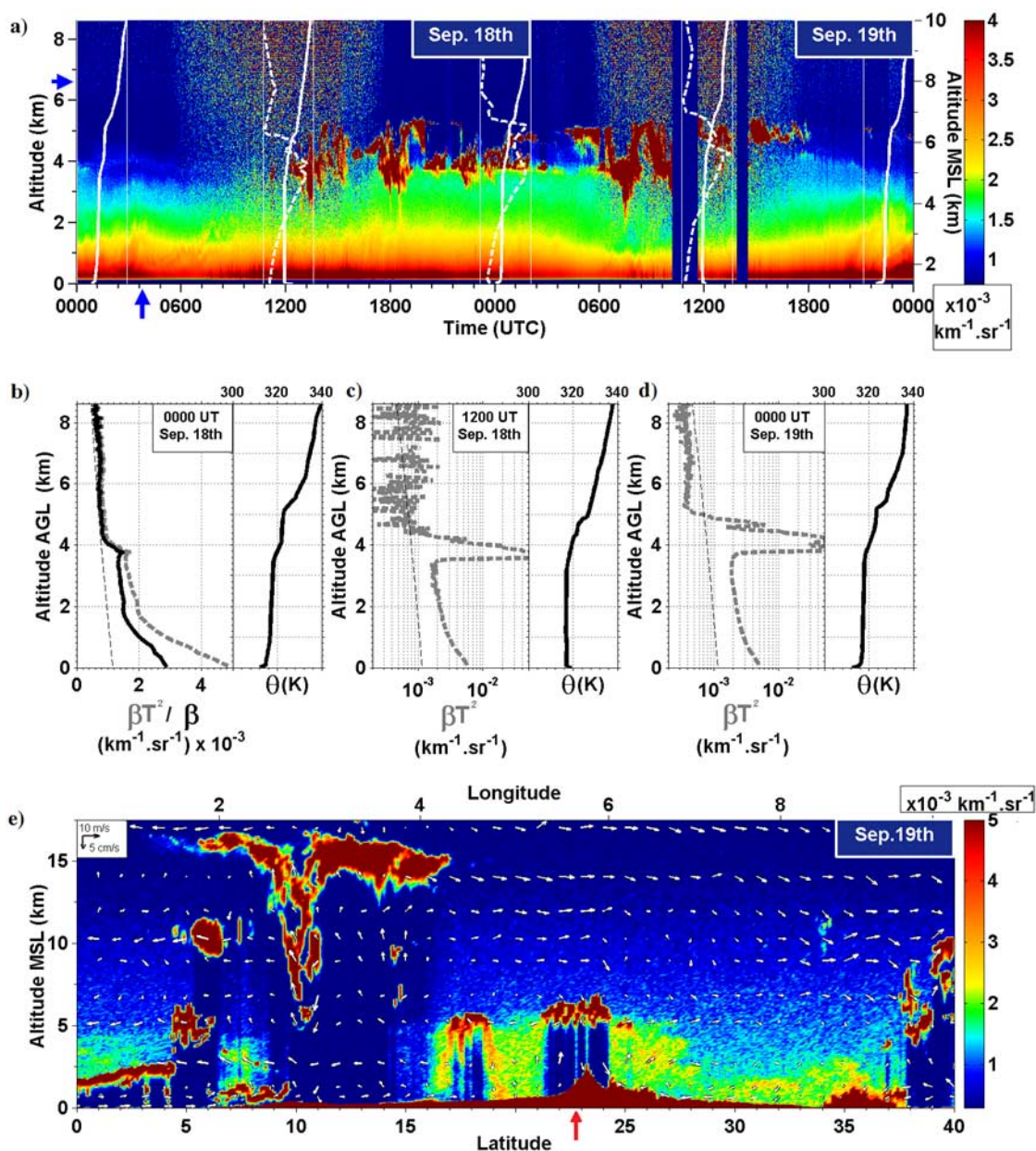


**Figure 11.** (a–e) Same as Figure 10 except for 18 and 19 September 2006 and only for the TReSS and CALIOP data. The CALIOP data shown are for 19 September at 0137 UTC.

respect to previously analyzed cases. In the upper troposphere, cirrus clouds were observed in the afternoon of 21 November between 8 and 13 km (see Figures 12a and 12c), below a tropopause located around 16 km MSL.

[53] As shown by CALIOP data over the Sahara (Figure 12e), nearly dust free conditions were observed over the Ahaggar region (from 18°N to 26°N the particle backscatter coefficient at 2 km MSL, obtained after inversion, was a factor  $\sim 5$  lower than on 25 June). The aerosol load was small over the Sahel and the Sahara. This was corroborated by the OMI aerosol index data, which exhibited small values ( $< 1$ ) over the whole Sahara (north of 18°N). Over sub-Saharan region (from 5°N to 13°N), a dense dust layer was observed from the surface up to 2 km MSL (see Figure 12e). OMI aerosol index values associated

with this dust layer were in excess of 3. The dust plume originated from the Bodélé depression, which remained active in the winter season.

## 7. Conclusions and Future Work

[54] Various mechanisms which directly affected the seasonal evolution of the SABL characteristics over Tamanrasset have been observed. The diurnal SABL development exhibited a large seasonal variation which was partly controlled by the seasonal evolution of several key features such as the dust load, monsoon-related moisture advections, large-scale subsidence and the proximity of the SHL. Moreover, the main observed meteorological forcing which caused dust events in Tamanrasset (i.e., cold pools

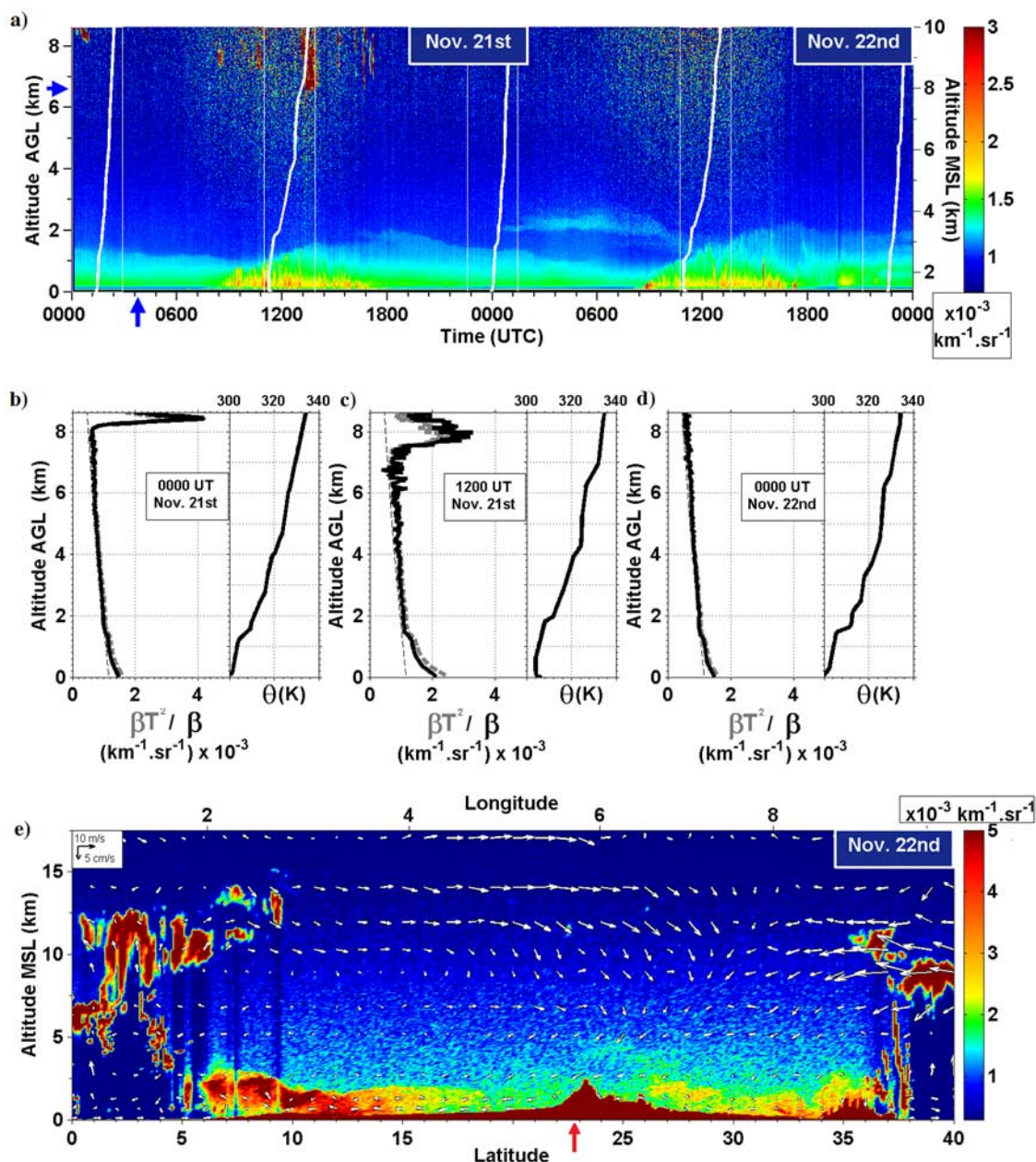


**Figure 12.** (a–e) Same as Figure 11 except for 21 and 22 November 2006. The CALIOP data shown are for 22 November at 0137 UTC.

generated by MCSs, low-level jets in source regions and topographic flows), the nonuniform distribution of dust within the CBL and the occurrence of dust updrafts and cloud downdrafts which intensified vertical recirculation within the SABL, were depicted. The analysis of the energy balance during the WAM onset phase period indicated an increase of the SABL growth and sensible heat flux around the so-called “dry onset,” followed by a sustained and significant decrease, as the actual WAM onset occurred.

[55] Further work is planned to study the influence of the SABL evolution, and the well documented prevailing conditions in Tamanrasset, on the SHL structure and intensity. The data acquired in Tamanrasset will also enable a quantification of the radiative impact of aerosols on the

energy budget through closure studies. Moreover, the relationship between the convective development of the SABL, in terms of the CBL depth and the entrainment zone thickness, is meant to be related to the variability of the sensible heat flux and the occurrence of dust events, particularly during the WAM onset period.

[56] **Acknowledgments.** On the basis of a French initiative, AMMA was built by an international scientific group and is currently funded by a large number of agencies, especially from France, UK, US, and Africa. It has been the beneficiary of a major financial contribution from the European Community’s Sixth Framework Research Programme. Detailed information on scientific coordination and funding is available on the AMMA International web site (<http://www.ammainternational.org>). The Tamanrasset AMMA supersite deployment was funded and supported by the Centre National d’Etudes Spatiales (CNES), the Action Programmatique

Inter-organismes (AMMA-API), the Office National de la Météorologie (ONM), and the Institut Pierre Simon Laplace (IPSL). The authors wish to thank E. Cuevas from the Instituto Nacional de Meteorología; a (INM), P. Chazette from Commissariat à l'Énergie Atomique (CEA), P. Goloub, L. Blarel, T. Podvin, M. Legrand, and B. Damiri from the Laboratoire d'Optique Atmosphérique (LOA), K. Desboeufs from the Laboratoire Interuniversitaire des Systèmes Atmosphériques (LISA), and L. Gomes from Météo-France for complementary radiometers, data, and technical support. The CALIPSO satellite data was supplied by D. Winker, L. Hunt, K. Morris, and M. Vaughan from NASA Langley ASDC User Services. The MSG/SEVIRI images were delivered by L. Gonzalez and C. Deroo from the LOA. Special thanks to A. Oulachidir, Y. Rouab, M. Salah Ferroudj, and M. Oumrana for their priceless support during the field campaign. The authors are grateful to A. Garnier, J. Pelon, and C. Lavaysse from the Service d'Aéronomie (SA) and M. Capderou from the Laboratoire de Météorologie Dynamique (LMD) for their suggestions and support for this work. The authors are indebted to M. Schaldembrand and the DT/INSU secretary for handling financial and travel matters.

## References

- Ackermann, J., P. Völger, and M. Wiegner (1999), Significance of multiple scattering from tropospheric aerosols for ground-based backscatter lidar measurements, *Appl. Opt.*, **38**, 5195–5201, doi:10.1364/AO.38.005195.
- Ångström, A. (1964), The parameters of atmospheric turbidity, *Tellus*, **16**, 64–75.
- Ati, O. F., C. J. Stigter, and E. O. Oladipo (2002), A comparison of methods to determine the onset of the growing season in northern Nigeria, *Int. J. Climatol.*, **22**, 731–742, doi:10.1002/joc.712.
- Bounoua, L., and T. N. Krishnamurti (1991), Thermodynamic budget of the five day wave over the Saharan desert during summer, *Meteorol. Atmos. Phys.*, **47**, 1–25, doi:10.1007/BF01025823.
- Caquineau, S., A. Gaudichet, L. Gomes, and M. Legrand (2002), Mineralogy of Saharan dust transported over northwestern tropical Atlantic Ocean in relation to source regions, *J. Geophys. Res.*, **107**(D15), 4251, doi:10.1029/2000JD000247.
- Cuesta, J., P. H. Flamant, and C. Loth (2004), Nouvelle Station d'Observations Transportable: Lidar et radiomètres, paper presented at Atelier d'Instrumentation et Experimentation 2004, Inst. Natl. des Sci. de l'Univers, Paris, 12–16 March.
- D'Almeida, G. A. (1986), A model for Saharan dust transport, *J. Clim. Appl. Meteorol.*, **25**, 903–916, doi:10.1175/1520-0450(1986)025<0903:AMFSDT>2.0.CO;2.
- D'Almeida, G., and L. Schültz (1983), Number, mass and volume distributions of mineral aerosol and soils of the Sahara, *J. Clim. Appl. Meteorol.*, **22**, 233–243, doi:10.1175/1520-0450(1983)022<0233:NMAVDO>2.0.CO;2.
- Dubief, J. (1959), *Le Climat du Sahara*, vol. I, 312 pp., Inst. de Rech. Sahariennes, Univ. d'Alger, Algiers.
- Dubief, J. (1963), *Le Climat du Sahara*, vol. II, 275 pp., Inst. de Rech. Sahariennes, Univ. d'Alger, Algiers.
- Dubief, J. (1979), Review of the North African climate with particular emphasis on the production of eolian dust in the Sahel Zone and in the Sahara, in *Saharan Dust: Mobilization, Transport, Deposition*, edited by C. Morales, pp. 27–48, John Wiley, Hoboken, N. J.
- Dubovik, O., and M. D. King (2000), A flexible inversion algorithm for retrieval of aerosol optical properties from Sun and sky radiance measurement, *J. Geophys. Res.*, **105**(D16), 20,673–20,696, doi:10.1029/2000JD900282.
- Dubovik, O., B. N. Holben, T. Lapyonok, A. Sinyuk, M. I. Mishchenko, P. Yang, and I. Slutsker (2002), Non-spherical aerosol retrieval method employing light scattering by spheroids, *Geophys. Res. Lett.*, **29**(10), 1415, doi:10.1029/2001GL014506.
- Fernald, F. G. (1984), Analysis of atmospheric lidar observations—Some comments, *Appl. Opt.*, **23**(5), 652–653.
- Fernald, F. G., B. M. Herman, and J. A. Reagan (1972), Determination of aerosol height distributions by lidar, *J. Appl. Meteorol.*, **11**, 482–489, doi:10.1175/1520-0450(1972)011<0482:DOAHDB>2.0.CO;2.
- Flamant, C., J.-P. Chaboureaud, D. J. Parker, and C. M. Taylor (2007), Airborne observations of the impact of a convective system on the planetary boundary layer thermodynamics and aerosol distribution in the inter-tropical discontinuity region of the West African monsoon, *Q. J. R. Meteorol. Soc.*, **133**(626), 1175–1189, doi:10.1002/qj.97.
- Hänel, G. (1976), The properties of atmospheric aerosol particles as functions of the relative humidity at thermodynamic equilibrium with the surrounding moist air, *Adv. Geophys.*, **19**, 73–188.
- Heffter, J. L. (1980), Air resources laboratories atmospheric transport and dispersion model, *NOAA Tech. Memo., ERL ARL-81*, 24 pp., Air Resour. Lab., NOAA, Silver Spring, Md.
- Heusinkveld, B., A. Jacobs, A. Holtslag, and S. Berkowicz (2004), Surface energy balance closure in an arid region: Role of soil heat flux, *J. Agric. For. Meteorol.*, **122**(1–2), 21–37.
- Holben, B. N., et al. (1998), AERONET—A federated instrument network and data archive for aerosol characterization, *Remote Sens. Environ.*, **66**, 1–16, doi:10.1016/S0034-4257(98)00031-5.
- Janicot, S., and B. Sultan (2007), The large-scale context on the West African monsoon in 2006, *Newsl. Clim. Variability Predict. Programme*, **12**(2), 11–12, 17. (Available at [http://eprints.soton.ac.uk/45355/01/Exchanges\\_41.pdf](http://eprints.soton.ac.uk/45355/01/Exchanges_41.pdf))
- Karyampudi, V. M., and T. N. Carlson (1988), Analysis and numerical simulations of the Saharan air layer and its effect on easterly wave disturbances, *J. Atmos. Sci.*, **45**(21), 3102–3136.
- Kaufman, Y., D. Tanré, J.-F. Léon, and J. Pelon (2003), Retrievals of profiles of fine and coarse aerosols using lidar and radiometric space measurements, *IEEE Trans. Geosci. Remote Sens.*, **41**(8), 1743–1754, doi:10.1109/TGRS.2003.814138.
- Knippertz, P., C. Deutscher, K. Kandler, T. Müller, O. Schulz, and L. Schütz (2007), Dust mobilization due to density currents in the Atlas region: Observations from the Saharan Mineral Dust Experiment 2006 field campaign, *J. Geophys. Res.*, **112**, D21109, doi:10.1029/2007JD008774.
- Loth, C., J. Cuesta, and P. H. Flamant (2004), TReSS: A transportable remote sensing station for atmospheric research and satellite validation, paper presented at 22nd International Laser Radar Conference, Int. Radiat. Comm., Int. Assoc. of Meteorol. and Atmos. Phys., Matera, Italy, 12–16 July.
- Marticoarena, B., and G. Bergametti (1995), Modeling the atmospheric dust cycle: 1. Design of a soil-derived dust emission scheme, *J. Geophys. Res.*, **100**(D8), 16415–16430, doi:10.1029/95JD00690.
- Measures, R. M. (1984), *Laser Remote Sensing: Fundamentals and Applications*, 524 pp., John Wiley, Hoboken, N. J.
- Oke, T. R. (1987), *Boundary Layer Climates*, 435 pp., Methuen, New York.
- Papayannis, A., et al. (2004), Saharan dust outbreaks towards Europe: 3 years of systematic observations by the European lidar network in the frame of the EARLINET project (2000–2003), paper presented at 22nd International Laser Radar Conference, Int. Radiat. Comm., Int. Assoc. of Meteorol. and Atmos. Phys., Matera, Italy, 12–16 July.
- Parker, D. J., and C. Flamant (Eds.) (2006), AMMA Task Team #8, SOP monsoon strategic planning document, Univ. of Leeds, Leeds, U. K. (Available at <http://amma-international.org/organisation/committees/taskteams/TT8/index>)
- Parker, D. J., R. R. Burton, A. Diongue-Niang, R. J. Ellis, M. Felton, C. M. Taylor, C. D. Thorncroft, P. Bessemoulin, and A. M. Tomkins (2005a), The diurnal cycle of the West African monsoon circulation, *Q. J. R. Meteorol. Soc.*, **131**, 2839–2860, doi:10.1256/qj.04.52.
- Parker, D. J., C. D. Thorncroft, R. R. Burton, and A. Diongue-Niang (2005b), Analysis of the African easterly jet, using aircraft observations from the JET2000 experiment, *Q. J. R. Meteorol. Soc.*, **131**, 1461–1482, doi:10.1256/qj.03.189.
- Peyrillé, P., and J. P. Lafore (2007), An idealized two-dimensional framework to study the West African monsoon, part II: Large scale advection and the diurnal cycle, *J. Atmos. Sci.*, **64**, 2783–2803, doi:10.1175/JAS4052.1.
- Peyrillé, P., J. P. Lafore, and J. L. Redelsperger (2007), An idealized two-dimensional framework to study the West African monsoon, part I: Validation and key controlling factors, *J. Atmos. Sci.*, **64**, 2765–2782, doi:10.1175/JAS3919.1.
- Prospero, J. M., P. Ginoux, O. Torres, S. E. Nicholson, and T. E. Gill (2002), Environmental characterization of global sources of atmospheric soil dust identified with the NIMBUS 7 Total Ozone Mapping Spectrometer (TOMS) absorbing aerosol product, *Rev. Geophys.*, **40**(1), 1002, doi:10.1029/2000RG000095.
- Ramel, R., H. Gallée, and C. Messenger (2006), On the northward shift of the west African monsoon, *Clim. Dyn.*, **26**, 429–440, doi:10.1007/s00382-005-0093-5.
- Redelsperger, J.-L., C. Thorncroft, A. Diedhiou, T. Lebel, D. Parker, and J. Polcher (2006), African Monsoon Multidisciplinary Analysis: An international research project and field campaign, *Bull. Am. Meteorol. Soc.*, **87**(12), 1739–1746, doi:10.1175/BAM-87-12-1739.
- Reid, J., D. Westphal, J. Livingston, D. Savoie, H. Maring, H. Jonsson, D. Eleuterio, J. Kinney, and E. Reid (2002), Dust vertical distribution in the Caribbean during the Puerto Rico Dust experiment, *Geophys. Res. Lett.*, **29**(7), 1151, doi:10.1029/2001GL014092.
- Rood, M. J., D. S. Covert, and T. V. Larson (1987), Hygroscopic properties of atmospheric aerosol in Riverside, California, *Tellus, Ser. B*, **39**, 383–397.
- Schotanus, P., F. T. M. Nieuwstadt, and H. A. R. de Bruin (1983), Temperature measurement with a sonic anemometer and its application to heat and moisture fluxes, *Boundary Layer Meteorol.*, **26**, 81–93, doi:10.1007/BF00164332.

- Shao, Y. (2000), *The Physics and Modelling of Wind Erosion*, pp. 127–128, Kluwer, Dordrecht, Netherlands.
- Stull, R. (1988), *An Introduction to Boundary Layer Meteorology*, Springer, New York.
- Sultan, B., and S. Janicot (2000), Abrupt shift of the ITCZ over West Africa and intra-seasonal variability, *Geophys. Res. Lett.*, *27*(20), 3353–3356, doi:10.1029/1999GL011285.
- Sultan, B., and S. Janicot (2003), The West African monsoon dynamics. Part II: The pre-onset and onset of the summer monsoon, *J. Clim.*, *16*, 3407–3427, doi:10.1175/1520-0442(2003)016<3407:TWAMDP>2.0.CO;2.
- Tanré, D., J. Haywood, J. Pelon, J. F. Léon, B. Chatenet, P. Formenti, P. Francis, P. Goloub, E. J. Highwood, and G. Myhre (2003), Measurement and modeling of the Saharan dust radiative impact: Overview of the Saharan Dust Experiment (SHADE), *J. Geophys. Res.*, *108*(D18), 8574, doi:10.1029/2002JD003273.
- Todd, M. C., R. Washington, S. Raghavan, G. Lizcano, and P. Knippertz (2008), Regional model simulations of the Bodélé low-level jet of northern Chad during the Bodélé Dust Experiment (BoDEx 2005), *J. Clim.*, *21*(5), 995–1012.
- Washington, R., M. C. Todd, S. Engelstaedter, S. Mbainayel, and F. Mitchell (2006), Dust and the low-level circulation over the Bodélé Depression, Chad: Observations from BoDEx 2005, *J. Geophys. Res.*, *111*, D03201, doi:10.1029/2005JD006502.
- Winker, D. M., J. Pelon, and M. P. McCormick (2003), The CALIPSO mission: Spaceborne lidar for observation of aerosols and clouds, *Proc. SPIE Int. Soc. Opt. Eng.*, *4893*, 1–11.
- Winker, D. M., W. H. Hunt, and M. J. McGill (2007), Initial performance assessment of CALIOP, *Geophys. Res. Lett.*, *34*, L19803, doi:10.1029/2007GL030135.
- Xiao, J., and P. Taylor (2002), On equilibrium profiles of suspended particles, *Boundary Layer Meteorol.*, *105*, 471–482, doi:10.1023/A:1020395323626.
- 
- A. Bouklila, M. Kharef, M. Mimouni, and B. Ouchène, Centre Tamanrasset, Office National de la Météorologie, 11000 Tamanrasset, Algeria.
- J. Cuesta, D. Edouart, P. H. Flamant, F. Gibert, C. Loth, and F. Marnas, Laboratoire de Météorologie Dynamique, Institut Pierre Simon Laplace, École Polytechnique, F-91128 Palaiseau, France. (cuesta@lmd.polytechnique.fr)
- C. Flamant, Service d'Aéronomie, Institut Pierre Simon Laplace, 4 Place Jussieu, F-75252 Paris, France.
- M. Kadi, Centre Alger, Office National de la Météorologie, 1, Avenue Mohamed Khemisti, 16012 Algiers, Algeria.